# FLEXIBLE PHOTOSENSING DEVICES

M.Sc. Thesis

By

# **Vaibhav Pratap Singh**

(Roll Number: 2303151029)



Under the guidance of

Dr. Onkar S. Game

**Department of Physics** 

**Indian Institute of Technology Indore** 

May 2025

# FLEXIBLE PHOTOSENSING DEVICES

#### A THESIS

Submitted in partial fulfillment of the requirements for the award of the degree

of

Master of Science

By Vaibhav Pratap Singh

(Roll Number: 2303151029)



Department of Physics

Indian Institute of Technology Indore

May 2025



#### INDIAN INSTITUTE OF TECHNOLOGY INDORE

#### CANDIDATE'S DECLARATION

I hereby certify that the work which is being presented in the thesis entitled **FLEXIBLE PHOTOSENSING DEVICES** in the partial fulfillment of the requirements for the award of the degree of **MASTER OF SCIENCE** and submitted in the **DEPARTMENT OF PHYSICS**, **Indian Institute of Technology Indore**, is an authentic record of my own work carried out during the time period from August 2023 to May 2025 under the supervision of **Dr. Onkar S. Game**, Assistant Professor, Department of Physics, IIT Indore.

The matter presented in this thesis has not been submitted by me for the award of any other degree of this or any other institute.

Librar Bratap Singh 21/05/2025 Signature of the student with date

(Vaibhav Pratap Singh)

This is to certify that the above statement made by the candidate is correct to the best of my/our knowledge.

Signature of the Supervisor of

M.Sc. thesis (with date)
(Dr. Onkar S. Game)

Vaibhav Pratap Singh has successfully given his M.Sc. Oral Examination held on May 2025.

Signature of DPGC Convener 21-05-25 (with date)

Sepankar Sas

(DPGC Convener)

Karmanye-vadhikaraste Ma Phaleshu Kadachana,
Karma Phala Hetur Bhur Ma Te Sango Stv Akarmani!
Dedicated to the Almighty, Lord Vishnu

# Acknowledgment

I would like to extend my deepest gratitude to my thesis supervisor, **Dr. Onkar S. Game**, for his invaluable guidance and support throughout my M.Sc. project. His consistent encouragement, thoughtful insights, and dedicated mentorship have played a pivotal role in the successful completion of this work. Beyond the project itself, his influence has significantly shaped my academic development, for which I am truly indebted.

I am also thankful to **Prof. Rupesh S. Devan** and his research group, Nano-architecture Research Group (NRG) from the MEMS Department at IIT Indore for granting me some useful facilities and equipments for the experiments. Equally, I am grateful to the Department of Physics, which provided me a platform to follow up my degree.

I admire my fellow labmates, **Miss. Aayushi Miglani**, **Mr. Shyam Lal Gurjar** and my friend **Mr. Aviral Upadhyay** from Advanced Energy Material and Devices (AEMD) research group for their help and support.

I am specially indebted to my mother, **Mrs. Anita Rani**, sister, **Miss. Divya Rajput**, father **Mr. Jaidrath Singh** and other relatives for their unconditional love, support, and fueling my academic journey. I am blessed to receive ongoing emotional support and continuous motivation from **Miss. Tanu Chauhan**.

### **Abstract**

Photodetectors(PDs) have many important applications in various fields; there is always a race to make them better and advanced. However, typical PDs are made of Si, GaAs, or some other semiconductors, and they are fragile. Recently, researchers discovered some inorganic-organic (hybrid) halide perovskite materials, which show enhanced parameters for optoelectronic applications. Since perovskites are flexible too, they fall into our main interest of making flexible photosensing devices.

This M.Sc. project has two tasks, one is to fabricate a PD device on a flexible substrate and another is to deliver concept of proof of their application in real life. For the convincing of reader, we have divided our work into small sections. These sections contains a good amount of information about PDs, their working principle, and figures of merit. We also extended this introduction part to the perovskites. Then, we have discussed the characterization methods that are useful for our purpose. After that, we explained the experiments in greater detail, our failures, and our success and presented the corresponding data. We successfully fabricated a flexible PD, and in the last section, we have shown how it can be used as a Photoplethysmogram (PPG) device. This is an important aspect for wearable electronics and real time health monitoring device.

# **Contents**

1	Intr	oductio	n	11
	1.1	History	y of Photodetectors	11
	1.2	Worki	ng Principles of Photodetectors	12
		1.2.1	Photoelectric Effect	12
		1.2.2	Photovoltaic Effect	13
		1.2.3	Photoconductivity	13
	1.3	Types	of Photodetectors	13
		1.3.1	Photoconductors	13
		1.3.2	Photodiodes	14
		1.3.3	Phototransistors	15
		1.3.4	Photomultiplier Tubes (PMTs)	15
		1.3.5	Thermopiles	16
	1.4	Figure	s of Merit for Photodetectors	16
		1.4.1	Responsivity	17
		1.4.2	External Quantum Efficiency (EQE)	17
		1.4.3	Response time	17
		1.4.4	Bandwidth	18
		1.4.5	Noise equivalent power (NEP)	19
		1.4.6	Specific Detectivity $(D^*)$	19
		1.4.7	On/Off ratio	19
		1.4.8	Linear Dynamic Range (LDR)	19
		1.4.9	Gain	20
	1.5	Perovs	kites	20
		1.5.1	Introduction	20

	1.6	Proper	ties of Perovskites	21
		1.6.1	High Absorption Coefficient	21
		1.6.2	Tunable Bandgap	21
		1.6.3	High Power Conversion Efficiency	22
		1.6.4	Long Carrier Diffusion Length	22
		1.6.5	Flexible Fabrication	22
		1.6.6	Photoluminescence and Electroluminescence	22
		1.6.7	Defect Tolerance	22
		1.6.8	Ambipolar Charge Transport	23
	1.7	Usages	s of Perovskites in Flexible Photodetectors	23
	1.8	Archite	ecture of Device:	24
		1.8.1	Lateral Configuration:	24
		1.8.2	Vertical Configuration:	25
2	Cha	racteriz	zation Techniques	27
	2.1	X-Ray	Diffraction	27
	2.2	Scanni	ng Electron Microscopy (SEM)	27
	2.3	UV-Vi	sible Diffusive Reflectance Spectroscopy	28
3	Exp	eriment	tal Section	29
	3.1	Fabrica	ation Procedure	29
		3.1.1	Substrate cleaning	29
		3.1.2	Precursor solution preparation	30
		3.1.3	Spin coating	31
	3.2	8.2 Experimental Work Stage 1:		32
		3.2.1	Characterization & Results and Discussion	33
	3.3	Experi	ment Stage 2	42
		3.3.1	Characterization & Results and Discussion	44
	3.4	Experi	mental Stage 3	53
		3.4.1	Trial 1 (failed!):	53
		3.4.2	Characterization, Results & Discussion	53
		3.4.3	Trial 2 (failed!)	59

5	Con	clusion		70
		4.1.1	Obtaining PPG waveform by our fexlible PD	67
	4.1	Photop	olethysmography	66
4	App	lication	(PPG sensor)	66
		3.4.5	Characterization, Results & Discussion	61
		3.4.4	Trial 3 (succeed!)	60

# **List of Figures**

1.1	Photoconductor [2]	14
1.2	Photodiode [2]	14
1.3	Phototransistor [2]	15
1.4	Photomultiplier Tube [3]	16
1.5	Thermopile [4]	16
1.6	Response of Photodetector under illumination and without illumination $[5]$	18
1.7	Perovskite Crystal Structure[10]	21
1.8	Basic Components of Flexible Photodetector[2]	23
1.9	Lateral Configuration of Photodetector	25
1.10	NIP-structure	25
1.11	Energy level diagram of different layers	26
3.1	Substrate Cleaning	30
3.2	Schematic diagram of 2-step Spin Coating	31
3.3	Schematic diagram of Spin Coating and Antisolvent quenching	32
3.4	Spin Coating process for Lateral Configuration	33
3.5	Snapshots taken during the process	33
3.6	XRD data of the sample	34
3.7	SEM images of FAPbI $_3$ surface with different magnifications	35
3.8	Grain size distribution of FAPbI $_3$ crystal	36
3.9	BSE and EDS data of $FAPbI_3$	37
3.10	Bandgap of FAPbI $_3$ calculated from UV-Vis DRS data $\ \ldots \ \ldots \ \ldots \ \ldots$	38
3.11	Photo response of the device at different wavelengths	39
3.12	Responsivity of the device	39
3.13	External coulombic efficiency of the device	40

3.14	Specific Detectivity of the device $D^*$	41
3.15	Snapshots taken during the device fabrication of triple cation composition	43
3.16	XRD pattern of $Cs_xFA_{(1-x-y)}MA_yPbI_{3-z}Br_z$	44
3.17	Bandgap of triple cation calculated from UV-Vis data	45
3.18	SEM images of $Cs_xFA_{(1-x-y)}MA_yPbI_{3-z}Br_z$ surface with different magnifica-	
	tions	46
3.19	Grain size distribution of $Cs_xFA_{(1-x-y)}MA_yPbI_{3-z}Br_z$ crystal	47
3.20	Response time of $Cs_xFA_{(1-x-y)}MA_yPbI_{3-z}Br_zPD$ (correction: J unit= $\mu Amp/cm^2$ )	) 48
3.21	I-V characteristics of $Cs_xFA_{(1-x-y)}MA_yPbI_{3-z}Br_z PD \dots \dots$	49
3.22	Responsivity of the device	50
3.23	External coulombic efficiency of the $Cs_xFA_{(1-x-y)}MA_yPbI_{3-z}Br_z$ device	51
3.24	Specific Detectivity of the device D*	52
3.25	Chuck with multiple holes	53
3.26	XRD pattern of $FA_{1-x}MA_xPbI_3$ coated on PET substrate	54
3.27	SEM images of $FA_{1-x}MA_xPbI_3$ coated on PET substrate	55
3.28	Grain size distribution of $FA_{1-x}MA_xPbI_3$ (coated on PET)	56
3.29	BSE and EDS data of $FA_{1-x}MA_xPbI_3$ (coated on PET)	57
3.30	IV curve of $FA_{1-x}MA_xPbI_3$ (coated on PET)	58
3.31	Failed fabrication of triple cation composition on PET substrate	59
3.32	Images of well fabricated triple cation Perovskite film on PET substrate	60
3.33	SEM images of the triple cation composition coated on PET substrate	61
3.34	Grain size distribution of the triple cation composition coated on PET	62
3.35	Photoresponse of triple cation composition PD fabricated on PET substrate	63
3.36	Responsivity of the triple cation device fabricated on PET	63
3.37	EQE of the $Cs_xFA_{(1-x-y)}MA_yPbI_{3-z}Br_z$ device	64
3.38	Specific Detectivity of the device D*:	65
4.1	The photoelectric plethysmograph, from Hertzman's original setup	67
4.2	PPG waveform	67
4.3	Using 730nm (Red wavelength) in transmission mode for monitoring heart rate	68
4.4	PPG waveform obtained experimentally	69

5.1 Schematic diagram of a smart wearable electronic device [25] . . . . . . . . . . . . . 71

# **Chapter 1**

# Introduction

Photodetector, as the name suggests, is a device that can detect photons, i.e. radiation. PDs convert optical signals into electrical signals and are used to sense different wavelengths of light across the electromagnetic spectrum, including visible, infrared, and ultraviolet light. The range of the detectable spectrum depends directly on the bqandgap of the material used. Photodetectors play a vital role in various fields such as optical communication systems, imaging devices, medical instruments, and environmental sensors.

### 1.1 History of Photodetectors

The history of photodetectors dates back to the early 19th century, with key discoveries laying the foundation for their development. In 1829, Italian scientists **Leopoldo Nobili** and **Macedonio Melloni** made a crucial observation related to infrared detection. They found that a thermocouple, an electrical device used to measure temperature, was sensitive enough to detect the heat emitted by a human body. This phenomenon would later be understood as the detection of infrared radiation using a thermopile, a precursor to modern thermal and infrared detectors.

However, the more direct birth of the photodetector is commonly attributed to **W.**Smith in 1873, when he discovered photoconductivity in selenium. Photoconductivity describes the process by which a material becomes more electrically conductive when illuminated. This discovery demonstrated that selenium could convert light into an electrical signal, a breakthrough that directly linked light sensing to electrical measurement, and laid the groundwork for the development of modern photodetectors. But still the process was slow until a major breakthrough occurred in 1905 when **Albert Einstein** provided a revolutionary explanation of the photoelectric effect. This explanation depends on the concept of **quanta of light**, which

was introduced by **Max Planck** in 1900 to solve the problem of **Blackbody radiation**[1].

As the new technologies for sensing the photon entered the picture, their application-based devices were also being developed. Smith's work opened the door to the development of photoelectric devices, such as early **photocells** and **photoresistors**. Over a span of 30 years, significant advancements were made in the development of photoelectric vacuum tubes, encompassing a wide range of detection applications. Notable innovations included the orthicon, often regarded as the precursor to modern image pickup devices, along with image converters, intensifiers, and the photomultiplier tube. The latter remains in use today due to its exceptional sensitivity, particularly for detecting single photons and elusive nuclear particles such as solar neutrinos. After World War  $2^{nd}$ , the understanding of solid state was improved and, resulted many semiconductor-based devices were invented. It also helped to develop semiconductor-based photodetectors with improved performance, reliability, spectral coverage, and size. Our work focuses on perovskite (a class of semiconductors) based photodetectors.

# 1.2 Working Principles of Photodetectors

The working principle of a photodetector is based on the **photoelectric effect**, **photovoltaic effect** or **photoconductivity**, where incident photons excite electrons in a material; these electrons create flow of current into the combined electronic circuit. In essence, this principle relies on a material absorbing light and subsequently emitting electrons, generating a current that varies in proportion to the light's intensity. Whereas, in the photoelectric effect, electrons are released from material's surface, typically a metal; when the radiation falls on it with appropriate energy.

#### 1.2.1 Photoelectric Effect

When a metal is exposed to light, electrons take the energy from the photos and they come out free from its surface; this phenomenon is known as the photoelectric effect. When light falls on the surface of a material, it can give its energy to the electrons in the material. If the energy of the incoming photon is high enough for the electron to overcome the binding energy (Workfunction) that holds them in the surface; then electron is ejected from the material. The electrons that are ejected are called **photoelectrons**.

#### 1.2.2 Photovoltaic Effect

Photovoltaic effect refers to the process of generating a voltage or current with the exposure of light through the electron-hole pair generation. Photon's energy excites the electrons, allowing them to move from the **valence band**, here electrons are bound to atoms to the **conduction band**, here electrons are free to move. This leaves a hole behind in the valence band. The photovoltaic effect is closely related to the photoelectric effect, but instead of ejecting electrons from a material, it creates a voltage (and a current if connected to a circuit). This effect occurs primarily in semiconductors.

#### 1.2.3 Photoconductivity

Photoconductivity is the effect of enhancing the electrical conductivity of a material when it is exposed to light. This happens when photons are absorbed by a material, leading to the generation of additional charge carriers (electrons and holes), which in turn increases the material's ability to conduct electrical current. These materials are called **photoconductive** materials.

### **1.3** Types of Photodetectors

According to the working principle, architecture, and modes of applications, there are the following types of photodetectors mainly:

#### 1.3.1 Photoconductors

**Principle:** Operating principle of a photoconductor is photoconductive effect, where the conductivity increases when it is exposed to radiation. The increment in conductivity is directly proportional to the intensity of radiation.

Materials: Cadmium sulfide (CdS) and lead sulfide (PbS) are commonly used.

**Applications:** Used in devices like automatic street lights, light meters, and exposure meters in photography.

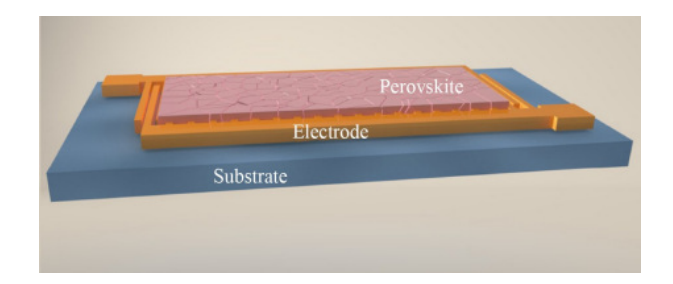


Figure 1.1: Photoconductor [2]

#### 1.3.2 Photodiodes

**Principle:** Photodiodes are basically p-n junction diodes that convert light into an electrical current through the photovoltaic effect. When radiation, having equal or more energy than the bandgap, falls on the diode, it generates electron and hole pairs. However, the pair, which is generated at the p-n junction, is drifted by the junction potential.

#### **Types of Photodiodes:**

- p-n junction photodiodes: It is simply made by combining p-type and n-type semiconductors together.
- Photodiodes: It has an intrinsic layer between the p and n regions, which increases the area of absorption. It helps to detect low-intensity radiation.
- Photodiodes (APDs): It operates in reverse bias and provides internal signal amplification due to avalanche multiplication, which increases sensitivity, but it also adds noise.

**Applications:** It is used in fiber-optic communication, light meters, barcode scanners, and environmental monitoring.

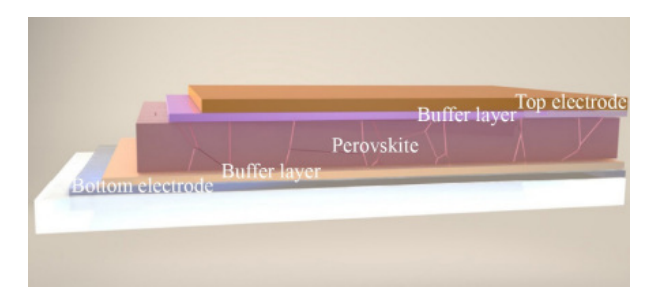


Figure 1.2: Photodiode [2]

#### 1.3.3 Phototransistors

**Principle:** A phototransistor is a bipolar junction transistor (BJT) (or a field-effect transistor FET) that can produce current by incident radiation. The incident radiation falls on the base-Collector junction and generates a voltage difference because of the photovoltaic effect, which is similar to a photodiode but with built-in amplification. The current generated by the radiation is amplified by the transistor.

**Advantages:** Phototransistors are highly sensitive and also become beneficial due to internal gain, which is not available in the photodiode. But it is slower comparatively.

**Applications:** Mainly phototransistors are used in light sensors, optical switches, and remote control receivers.

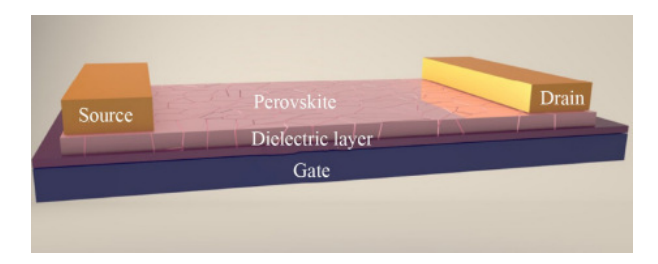


Figure 1.3: Phototransistor [2]

#### **1.3.4** Photomultiplier Tubes (PMTs)

**Principle:** PMTs are highly sensitive detectors that use the photoelectric effect to convert light into electrons. It has a series of dynodes, which multiply electrons whenever electrons strike the dynode, and hence it reflects the exponential increment in the number of electrons for every incident photon, leading to a very high gain.

**Advantages:** PMTs are extremely sensitive, which are capable to detect very low intensity of radiation (even a single photon). However, PMTs are costly and operate at high voltage. The size of PMT is also an issue.

**Applications:** PMTs are widely used in high-energy physics and astronomy. It is also useful for scientific research that requires low-light detection.

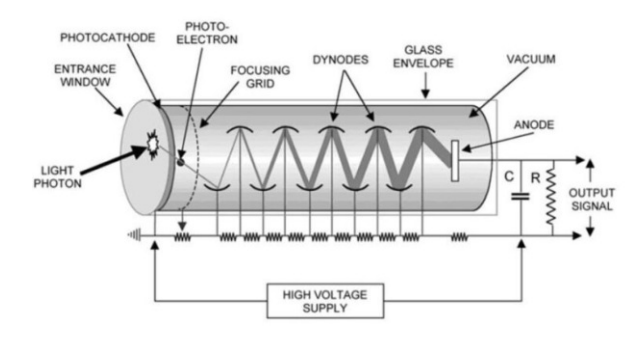


Figure 1.4: Photomultiplier Tube [3]

#### 1.3.5 Thermopiles

**Principle:** Thermopiles are based on the Seebeck effect, in which a temperature difference between two materials generates a voltage. Thermopile absorbs the infrared radiation, which causes a temperature difference and generates a measurable voltage.

**Applications:** Thermopiles can be used as infrared sensors and thermography.

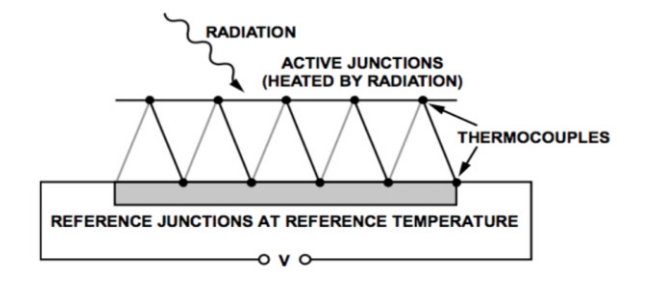


Figure 1.5: Thermopile [4]

There are some more types of photodetectors such as Charged Complementary Metal-Oxide-Semiconductor (CMOS) Image Sensors, Coupled Devices (CCDs), Quantum Dot Photodetectors, Photovoltaic Cells, Pyroelectric Detectors, Phototubes and Bolometers.

### 1.4 Figures of Merit for Photodetectors

This section is important as such parameters are described here, which are useful to characterize the performance of a photodetector and also allow comparison between two or more. These parameters basically depend on the absorption processes, electron-hole pair generation, and on the energy distribution of incident radiation, indeed. These characterization parameters are listed as follows:

#### 1.4.1 Responsivity

Responsivity quantifies how effectively the device converts incident light into an electrical signal (current or voltage). It is defined as the ratio of the output current (or voltage) to the incident optical power and is typically measured in **amperes per watt** (A/W) (or volts per watt (V/W), depending on whether the output is current or voltage).

Responsivity (R) = 
$$\frac{I_{ph}}{P_{in}}$$
 (1.1)

where,  $I_{ph}$  is the photocurrent generated by the photodetector and  $P_{in}$  is the incident optical power.

#### **1.4.2** External Quantum Efficiency (EQE)

External Quantum Efficiency (EQE) is the measure of how effectively a device converts incoming photons into collected electron-hole pairs, expressed as the ratio of collected charge carriers to the number of incident photons.

$$EQE = \frac{\text{total e-h collected}}{\text{total incident photon}} = R \frac{\hbar c}{q\lambda}$$
 (1.2)

(For a monochromatic radiation.)

#### **Meaning of EQE:**

If EQE = 100%, every photon incident on the photodetector results in the generation of a single electron-hole pair. This pair also contributes to the production of a photocurrent.

If EQE < 100%, fewer electron-hole pairs are generated than the number of incident photons, which means that some photons are either lost or not converted to charge carriers or generated electrons or holes were recombined and could not participate in the photocurrent.

If EQE > 100% it occurs in some cases, especially in devices like avalanche photodiodes (APDs), where internal amplification processes allow more than one charge carrier to be generated per incident photon.

#### 1.4.3 Response time

Response time defines the detection speed of the photodetector, that is, how fast the photodetector responds to incident light. This property plays a crucial role in various applica-

tions, including optical communication, high-speed light detection, and imaging sensors. The response time consists of **Rise Time** ( $\tau_{rise}$ ) and **Fall Time** ( $\tau_{fall}$ ).

Under illumination, the time it takes the photocurrent to reach 90% from 10% of its maximum is defined as  $\tau_{rise}$ . Similarly,  $\tau_{fall}$  is defined as the time taken for decaying photocurrent from 90% to 10% of its maximum when radiation is turned off. The response time is closely related to the charge transfer and charge collection process in a photodetector.

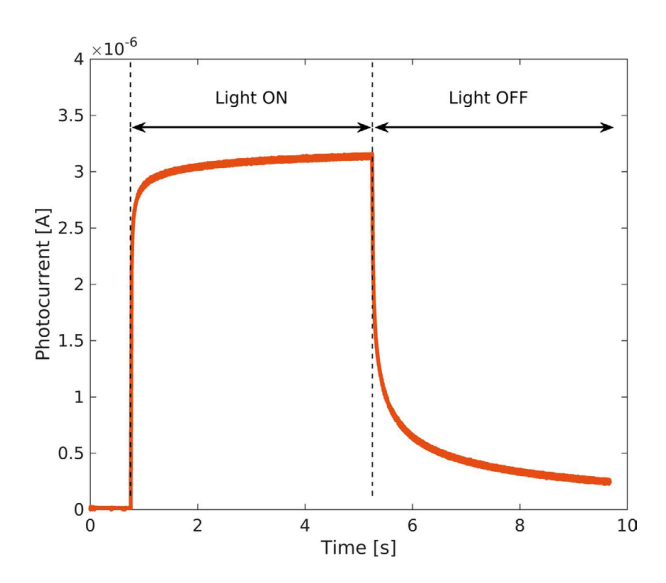


Figure 1.6: Response of Photodetector under illumination and without illumination[5]

#### 1.4.4 Bandwidth

Bandwidth becomes important for fast optical communication. To transfer data from one end to another, usually we modulate the signal frequency (here we are not talking about the frequency of photon, it is the frequency of signal that how fast it transmits the encoded data in the series of binary numbers. For example, for a large data file the series of 0&1 would be large and to transfer it in, a short time, the signal would have to go up and down more rapidly. Where getting up represents 1 and falling down represents 0).

Typically, bandwidth is measured between the frequencies where the output power drops by 3 dB from the maximum value. This is often referred to as the **3 dB bandwidth**. It is measured in **Hertz (Hz)**.

Bandwidth (B) 
$$\propto \frac{1}{\text{Response Time}}$$
 (1.3)

#### 1.4.5 Noise equivalent power (NEP)

NEP is defined as the minimum optical input power at which the signal-to-noise ratio becomes unit. It is a critical parameter that determines the ability to detect weak optical signals. It is measured in watts.

Noise equivalent power NEP = 
$$\frac{\sqrt{2qI_d + 4k_BT/r}}{R}\sqrt{B}$$
 (1.4)

Where,  $I_d$  is dark current, q is fundamental electronic charge, T is absolute temperature,  $k_B$  is Boltzmann constant, r is zero biased resistance, B is bandwidth.

#### 1.4.6 Specific Detectivity $(D^*)$

It is a fundamental parameter that represents the ability to detect weak optical signals. It is the inverse of the NEP, which is normalized by the detector area and the bandwidth. It makes the comparison easier of photodetectors with different sizes and configurations. The unit of measurement of the detectivity is **Jones**.

Specific Detectivity 
$$(D^*) = \frac{\sqrt{S} \sqrt{B}}{NEP}$$
 (1.5)

#### 1.4.7 On/Off ratio

In addition to detectivity, the on/off ratio is another key parameter that indicates a photodetector's sensitivity to light. It is determined by the ratio of the photocurrent  $(I_{ph})$  to the dark current  $(I_d)$  measured under identical conditions. A higher on/off ratio describes how effectively we detect the input signal.

On/Off Ratio = 
$$\frac{I_{Ph}}{I_d}$$
 (1.6)

#### 1.4.8 Linear Dynamic Range (LDR)

LDR reflects the range of incident power over which the photocurrent (or voltage) is linear in the logarithmic graph. It also describes the reliable power range of incident radiation.

#### 1.4.9 Gain

It is defined as the charge carriers collected per incident photon, which can be characterized by the ratio of the carrier lifetime ( $\tau_{lifetime}$ ) to the carrier transit time ( $\tau_{transit}$ ).

$$G = \frac{\tau_{lifetime}}{\tau_{transit}} = \frac{\mu \ V \tau_{lifetime}}{d^2}$$
 (1.8)

Where, d is the channel length of photodetector, V is the bias voltage,  $\mu$  is the carrier mobility.

#### 1.5 Perovskites

#### 1.5.1 Introduction

Perovskite is a different class of semiconductors; it became popular in recent decades because of its enhanced properties in photovoltaics over conventional semiconductors. These such properties are high absorption coefficient, tunable bandgap, low recombination losses, and so on. In addition, perovskites can be made by solution-based processes, which is an easier and cheaper method. Perovskite-based solar cells achieved around 26.7% power conversion efficiency[6], which is much better than Si-based solar cells. Perovskites are also useful for photodetectors, which helps to increase their performance. Keeping this in mind, researchers developed many photodetectors, based on perovskites[7]. However, perovskite materials have shown tremendous potential in the field of photovoltaics, but they also face several significant challenges, such as fast degradation, being less stable, toxicity, and ion migration. These problems need to be addressed before they can become a mainstream alternative to traditional materials such as silicon.

Perovskite was first identified in 1839 by the Prussian mineralogist **Gustav Rose**, who discovered it within a chlorite-rich skarn[8]. The mineral, composed of CaTiO<sub>3</sub>, was named in honor of the distinguished Russian mineralogist **Count Lev A. Perovskiy**[9]. The general formula for perovskites is AMX<sub>3</sub>. Where;

- A is a large cation (e.g. methylammonium, cesium, or formamidinium).
- M is a smaller cation (e.g., lead, tin).
- X is an anion, halide, or oxide.

M cation shows 6-fold coordination and it is surrounded by an octahedron of anions, while

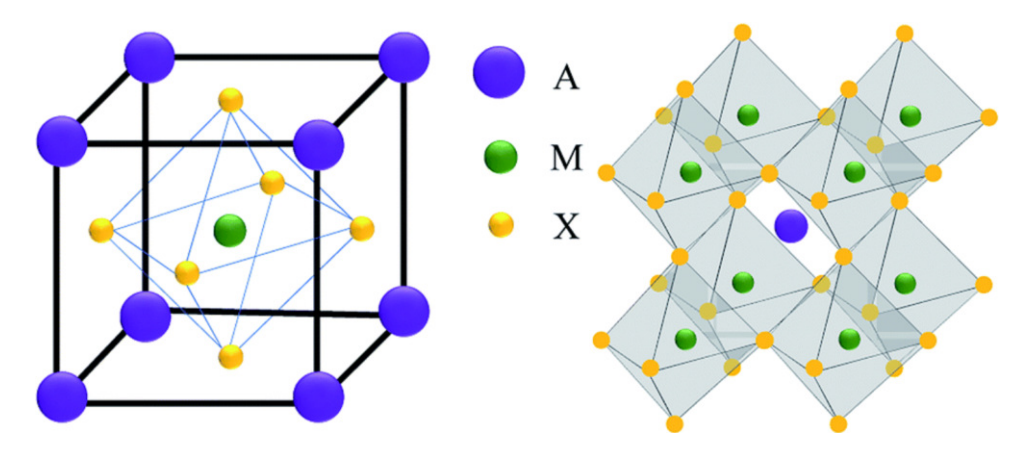


Figure 1.7: Perovskite Crystal Structure[10]

the A cation has 12-fold cuboctahedral coordination. Its cubic unit cell can be illustrated as A cation is positioned at the corners, X anions are present on the face centers, and B is positioned at the body center.

### 1.6 Properties of Perovskites

The properties which make perovskites important are listed below;

#### 1.6.1 High Absorption Coefficient

Absorption coefficient of a material defines the radiation absorption properties for that material. It is a function of the band gap and wavelength of incident radiation. Higher absorption coefficient means that the material can absorb a significant amount of radiation. Some perovskites have a higher absorption coefficient, which allows them to absorb much radiation. A thin film of perovskite (around 500 nm) can absorb more than 90% of sunlight, making it ideal for thin-film photovoltaics and light energy harvesting.

#### 1.6.2 Tunable Bandgap

Typically, bandgap of perovskites ranges from **1.2 eV** to **2.3 eV**. This bandgap can be tuned by altering the chemical compositions by changing halide or cations. The tunable bandgap allows us to make such photodetectors, which are useful for sensing the radiation of the required frequency range. It also helps perovskites to absorb different parts of the solar spectrum. Also, optical and electronic properties can be finely adjusted, which is beneficial for tandem solar cells or color-specific LEDs.

#### **1.6.3** High Power Conversion Efficiency

Perovskite solar cells have demonstrated rapid increases in power conversion efficiency (PCE), reaching over **26.7**%[10], which is higher than silicon solar cells. Perovskite solar cells exhibit high open-circuit voltages, which contributes to their high efficiency.

#### 1.6.4 Long Carrier Diffusion Length

Carrier diffusion length is referred to as the average distance traveled by the charge carriers before they recombine. Perovskites exhibit a long charge carrier diffusion length ( $10^{-6}$  to  $10^{-7}$  m), which reduces the probability of recombination and helps to increase the power conversion efficiency.

#### 1.6.5 Flexible Fabrication

Perovskites can be fabricated by solution-based processes (e.g., spin-coating, inkjet printing) which require low temperature (around 150°C) methods. Perovskites can be used as an active material as a thin film of them can be deposited on a flexible substrate. It makes perovskites suitable and a good choice for flexible and wearable electronics. This property is so important for our purpose of making flexible photosensing devices.

#### 1.6.6 Photoluminescence and Electroluminescence

Perovskites have strong photoluminescent and electroluminescent properties, making them ideal for applications in light-emitting devices such as LEDs. Perovskites can emit light with high colour purity, and their bandgap is tunable across the visible spectrum, from blue to red, by altering their halide composition.

#### 1.6.7 Defect Tolerance

Unlike traditional semiconductors, perovskites are relatively tolerant to defects in their crystal structure[11]. Defects usually act as trap states for electrons and holes, which reduces the number of carriers and hampers the efficiency. However, perovskites exhibit fewer performance losses from defects, which simplifies manufacturing.

#### 1.6.8 Ambipolar Charge Transport

Perovskites exhibit ambipolar transport properties, which means they can transport both electrons and holes efficiently. This property is beneficial for optoelectronic devices such as LEDs and solar cells, where charge balance is critical.

### 1.7 Usages of Perovskites in Flexible Photodetectors

Flexibility of perovskites is a key property which makes them suitable for flexible photodetectors, besides flexible substrate, electrode and encapsulation layer. Polycrystalline thin-film-based perovskites suffer from high bulk defects, large grain boundaries, and serious performance losses under operation (e.g. folding or bending). Low-dimensional perovskite processes are beneficial for single-crystalline perovskites, which have low-density bulk defects and fewer grain boundaries. It offers good and well mechanical flexibility too.

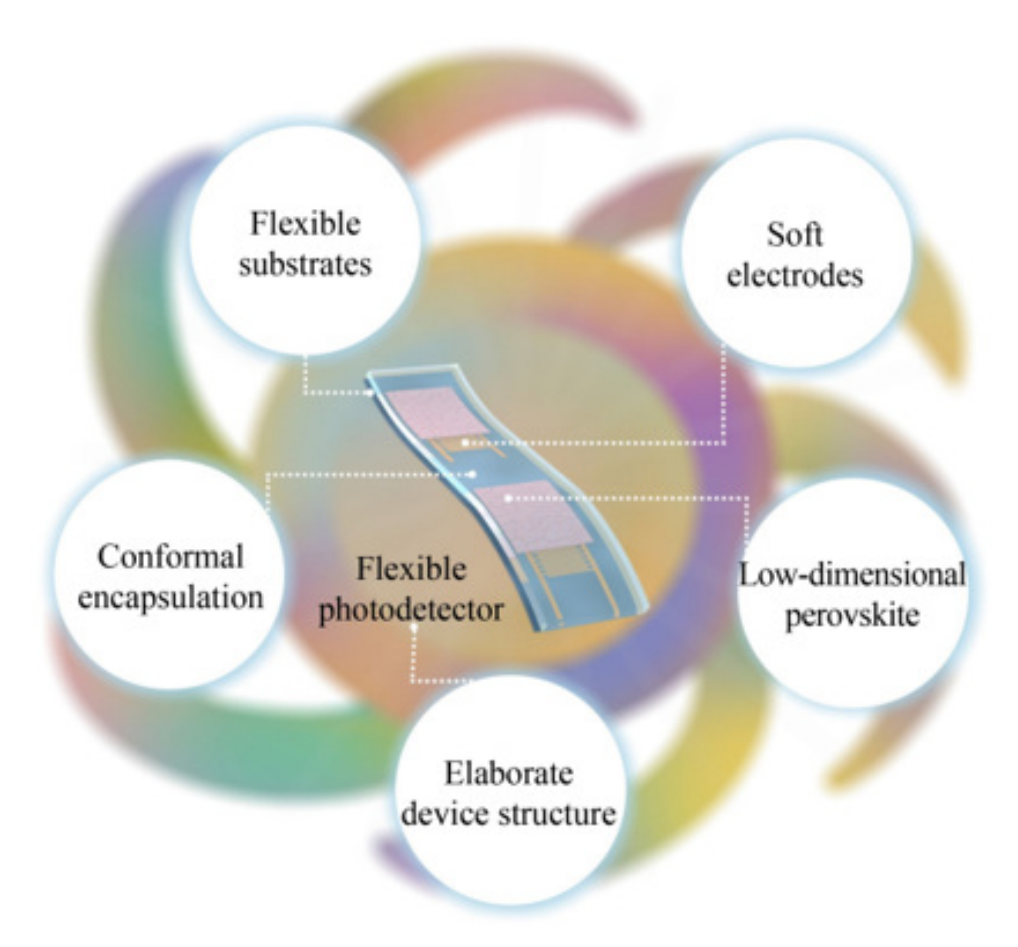


Figure 1.8: Basic Components of Flexible Photodetector[2]

According to size and dimensions, there are 3 types of low-dimension perovskites:

• **0-D particles:** 0-D particles consist mainly of nanocrystals and quantum dots. 0-D perovskite quantum dots and nanocrystal films exhibit superior light-harvesting ability than bulk material. It means 0-D perovskite film-based photodetectors have a higher photocurrent, on/off ratio, and responsivity. It is also reported that 0-D films showed outstanding flexibility and electrical stability, and thus 0-D perovskites have a great potential in fabrication of flexible devices. However, 0-D particles are isolated from each other; they have to suffer from poor interfacial carrier transport, which can be improved by using carbon nanotubes with quantum dots[13][14].

- 1-D nanostructures: 1-D nanostructures consist of nanowires and nanotubes, offering more direct charge transport than 0-D perovskites. Due to the virtue of low dimension, 1-D perovskites also show lower defects, resulting in a lower recombination rate and good mechanical flexibility. However, the nanowires network has many microinterfaces between nanowires, which abruptly the carrier transport and absorb water-oxygen molecules, which can cause a significant performance decay. A welding strategy can be used to reduce micro-interfaces and allow the nanowires to form a film without stacking[14].
- 2-D nanostructures: 2-D nanostructures consist of nano-flakes, or layers with atomic thickness, expected to have faster carrier transport in-plane, due to the absence of hopping barriers. 2D layered perovskite films can be fabricated using solution-based methods easily and cost effectively.

Hence, perovskites have magical properties that enhance the performance of photodetectors and solar cells. They are also fit for flexible electronics, and flexible photodetectors. We made thin film of perovskite as the active material for our photodetectors.

#### 1.8 Architecture of Device:

According to the method of fabrication, the photodetector can be made in the lateral and vertical configuration. However, it also makes differences in the operation of both.

#### 1.8.1 Lateral Configuration:

In this configuration, a layer of photoactive material (perovskite) is deposited between two horizontally placed electrodes (ITO) and continuous external electric field is applied across

this device. In the exposure to electromagnetic radiation, charge carriers are generated in the device. These carriers increase conductivity of the device and **it works as a photoconductor** (Section 1.3.1).

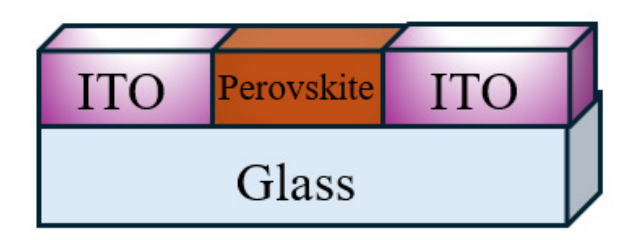


Figure 1.9: Lateral Configuration of Photodetector

#### **1.8.2** Vertical Configuration:

This configuration can be realized by putting active material (perovskite) between two vertically placed electrodes. Depending on the position of the positive and negative electrodes, this configuration can be further split into two, NIP and PIN structure. In our case, we are using NIP structure (Fig. 1.10). Along with the perovskite layer we are using layers of other materials, these layers are basically called Electron Transport Layer (ETL) and Hole Transport Layer (HTL); which facilitate extraction of electrons and holes, respectively (Fig. 1.11). **This PD warks as a photodiode**.

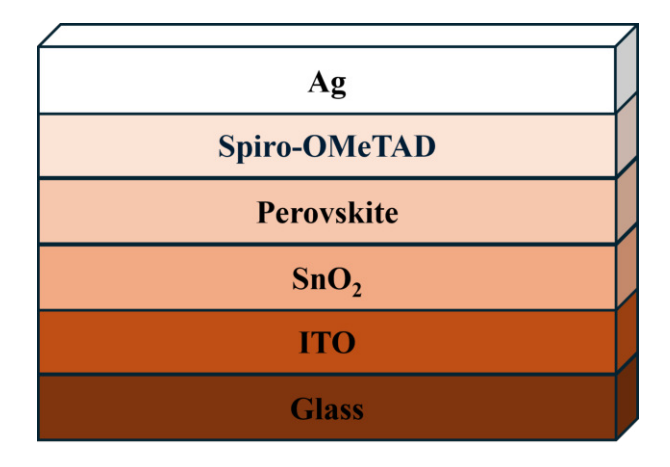


Figure 1.10: NIP-structure

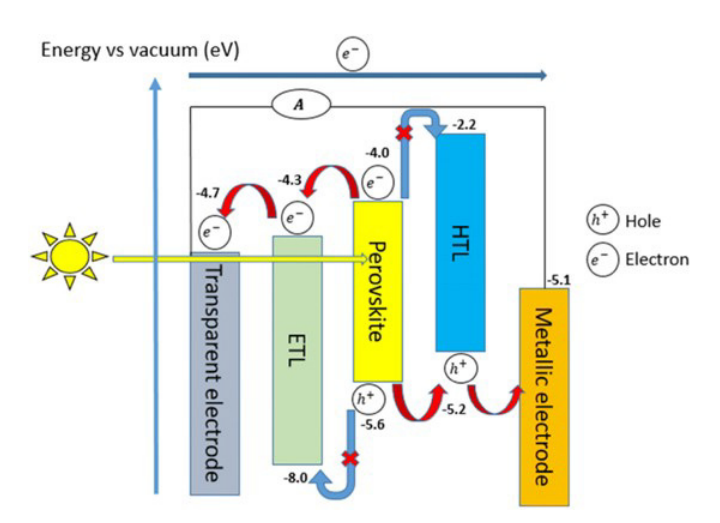


Figure 1.11: Energy level diagram of different layers

# **Chapter 2**

# **Characterization Techniques**

### 2.1 X-Ray Diffraction

XRD pattern is a signature of a material and helps to probe its crystal structure. X-rays are directed on the sample, and they get diffracted in a specific direction. Then, the angle and intensity of these diffracted X-rays is measured to make a diffraction pattern. A crystalline material represents sharp diffraction peaks in the plotted graph between the scattering angle  $(2\theta)$  and the intensity of the scattered radiation. This technique is useful to get information about crystal structure, phase , lattice parameters and other structural properties, based on Bragg's law.

$$2d\sin\theta = n\lambda\tag{2.1}$$

### 2.2 Scanning Electron Microscopy (SEM)

SEM is used to see the surface images of materials at very high magnifications (10x to 100x), with a resolution of 1nm-10nm. We focus a beam of electrons onto the surface of sample and see its surface, record other signals as well which are produced from this interaction of electrons with the sample. These electrons can be accelerated by 0.5 keV to 30 keV energy to examine different types of materials (for soft materials, lower energy electrons are used to avoid damage and higher energy electrons are useful for hard materials to penetrate deeper). This interaction provide us 3 main data, secondary electrons, back scattered electrons, and emitted X-rays. Secondary electrons are important to create high resolution image of the surface, while back scattered electrons inform about compositional differences as heavy atoms scatter more electrons and make brighter regions in the image. Inner shell electrons with high energy are ejected from the material, then electrons from outer shells fall into these empty

shells and emit radiation in X-ray range. These X-rays have the information of corresponding atoms and can be used to determine atoms by using Energy-Dispersive X-ray Spectroscopy (EDS) with SEM. Elements from Boron (Z=5) to Uranium (Z=92) can be detected using this method.

### 2.3 UV-Visible Diffusive Reflectance Spectroscopy

UV-Vis spectroscopy is analytical technique, used to study the absorption of UV and visible light (200-800nm) by the sample. This is useful for both liquid (solution) and solids and helps to determine the quantitative analysis of solutions (concentration) and the band gap of solids. It provides information about the electronic transition, which happens by the absorption of the photon when its energy matches with the energy gap of transition states and other photons are transmitted. But for the opaque and powder sample, which scatters light, diffusive reflectance is measured, and this technique is called Diffusive Reflectance Spectroscopy (DSR). The reflectance spectrum is converted to absorption like data by using Kubelka-Munk function:

$$F(R) = \frac{(1-R)^2}{2R} \tag{2.2}$$

where;

R: Diffuse reflectance of the sample,  $R = \frac{I_{reflected}}{I_{incident}}$ .

For semiconductors, plotting  $(F(R) \cdot hv)^n$  (where hv is the photon energy and n depends on the type of electronic transition). The extrapolation of the linear portion to the x-axis yields the bandgap energy.

# **Chapter 3**

# **Experimental Section**

#### 3.1 Fabrication Procedure

PDs were fabricated on glass or PET substrate by solution-processed fabrication of perovskite layer in lateral and vertical configuration. The fabrication steps are as following:

#### 3.1.1 Substrate cleaning

We use ITO (Indium Tin Oxide) coated glass and PET polymer as a substrate. Cleaning is a primary step and very important to the wellness of next steps. After making patterns by etching, substrates were cleaned with soap water at first and treated with ultrasonic waves while immersed in IPA and acetone at room temperature. Up to this pint, dust particles and other sticky contaminants were removed. Afterwards, the next step includes UV-ozone cleaning, which effectively removes organic contaminants to the atomic levels. The UV ozone method is safe and chemical-free, which enables to apply on a wide range of materials. It uses UV light at 185nm and 254 nm, which interacts with atmospheric oxygen and convert it into ozone (O<sub>3</sub>). Ozone is a potent oxidizing agent, which further attacks on organic compounds and decomposes them. This cleaned glass substrate is further transferred into N<sub>2</sub> filled glove box.

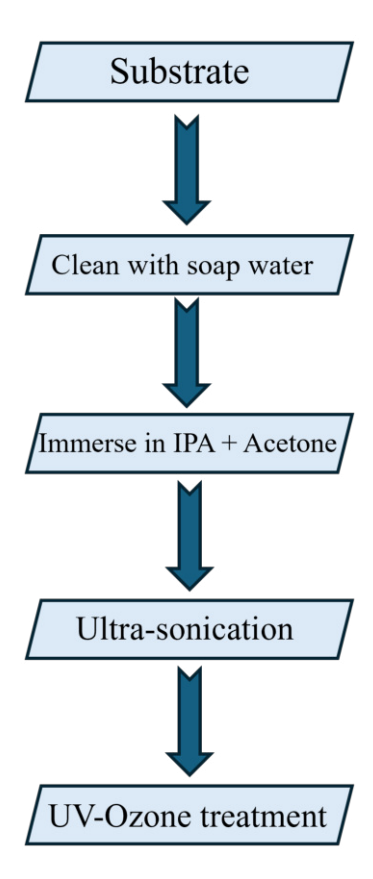


Figure 3.1: Substrate Cleaning

#### 3.1.2 Precursor solution preparation

We have tried two different compositions of organic-inorganic halide perovskites. The process of making solution is different for both and it is described as follows:

- Solution making for (FA<sub>1-x</sub>MA<sub>x</sub>PbI<sub>3</sub>): Formamidine Hydroiodide (CH<sub>5</sub>IN<sub>2</sub>, FAI, >99.995%), Methylammonium Iodide (CH<sub>6</sub>IN, MAI, >99.99%) and Lead (II) Iodide (PbI<sub>2</sub>, 99.99%) provided by TCI, are used for the formation of perovskite (FA<sub>1-x</sub>MA<sub>x</sub>PbI<sub>3</sub>). Used solvents are N,N-Dimethylformamide (DMF, anhydrous, 99.8%), Dimethyl sulfoxide (DMSO, anhydrous,  $\geq$  99.9%), tert-Butyl alcohol (TBA, anhydrous,  $\geq$  99.5%) manufactured by Sigma-Aldrich. We need to prepare solutions of them separately. The solution of PbI<sub>2</sub> is prepared in the mixture of DMF and DMSO, on the other hand, solution of FAI is prepared in TBA.
- Solution making for Triple cation provskite ( $Cs_xFA_{(1-x-y)}MA_yPbI_{3-z}Br_z$ ): We prepare two different solutions of precursors. In the solution 1, Formamidine Hydroiodide ( $CH_5IN_2$ , FAI, >99.99%), Lead(II) Iodide ( $PbI_2$ , 99.99%), Methylamine Hydrobromide ( $CH_6BrN$ , MABr, Low water content, purity >98%), Lead(II) Bromide ( $PbBr_2$ , >98%), all are provided by TCI, were dissolved in DMF (N,N-Dimethylformamide (anhydrous, 99.8%)) and DMSO (Dimethyl

sulfoxide (anhydrous,  $\geq 99.9\%$ )). The  $2^{nd}$  solution is prepared by dissolving Cesium Iodide (CsI, >99.0%) in DMSO. The second solution was mixed into the first one to dope the appropriate amount of Cs in the perovskite composition.

#### 3.1.3 Spin coating

Spin coating is chemical based deposition method, an easy way to fabricate perovskite layer. It provides an uniform layer and useful for small-scale production or for research purposes. Spin coating was also done in the different way for those two different compositions:

• For  $FA_{1-x}MA_xPbI_3$  composition: First, a layer of  $Sno_2$  (ETL) was spin-coated on the substrate and annealed at pre-heated hot plate at  $150^{\circ}C$  under ambient condition. After that,  $PbI_2$  solution was spin-coated onto it and annealed at  $65^{\circ}C$  in the  $N_2$  filled glove box. Following that, FAMAI solution was spin coated and annealed at  $150^{\circ}C$ . FAI and  $PbI_2$  react with each other and condensed into perovskite ( $\alpha$ -FAPbI<sub>3</sub>) phase, which is photoactive phase. This process is generally called two-step coating. After that, Spiro-OMeTAD was coated onto it which acts as HTL layer.

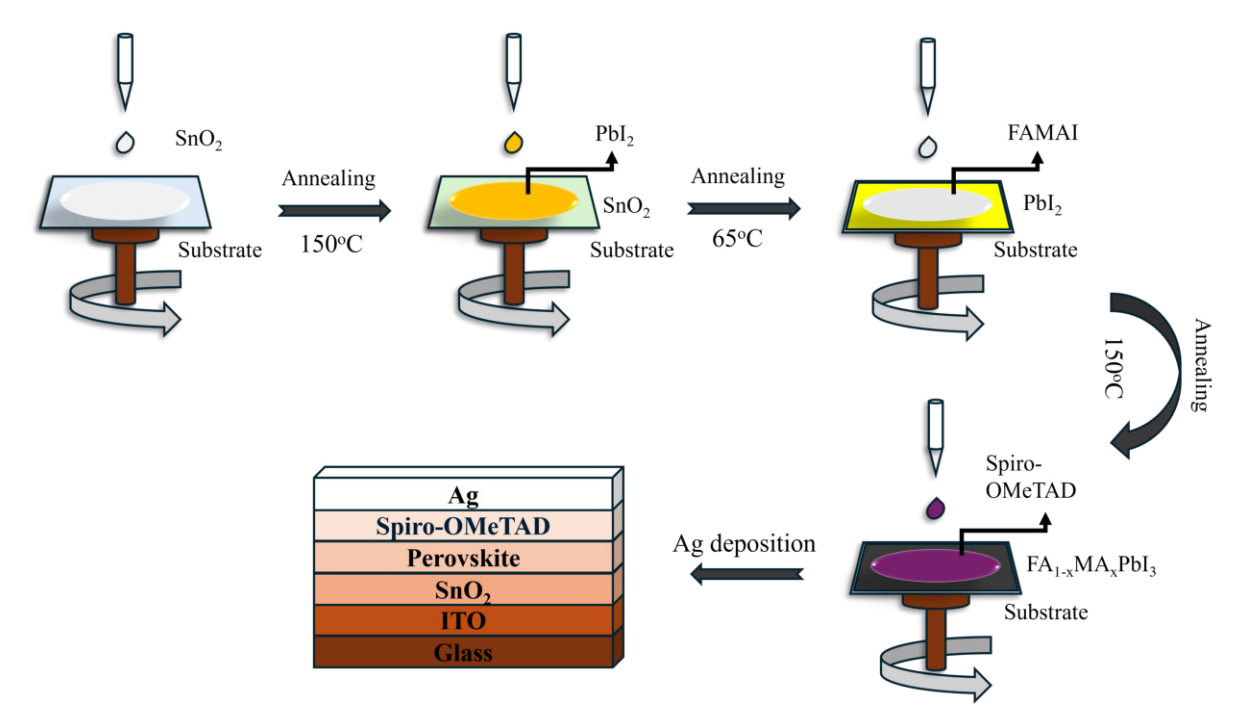


Figure 3.2: Schematic diagram of 2-step Spin Coating

• For Triple Cation ( $Cs_xFA_{(1-x-y)}MA_yPbI_{3-z}Br_z$ ) composition: The same process was done upto  $SnO_2$  coating, then a layer of mixed triple cation precusor solution was deposited on the substrate and spin coated on it. During this coating, Chlorobenzene was dropped, which acts

as an anti-solvent and creates nucleation centers of the perovskite immediately. This method is known as anti-solvent quenching. Then coated substrates were annealed at  $100^{\circ}$ C for 20 minutes. Then, Spiro-OMeTAD was coated onto it. All of these processes were done in  $N_2$  filled glove box.

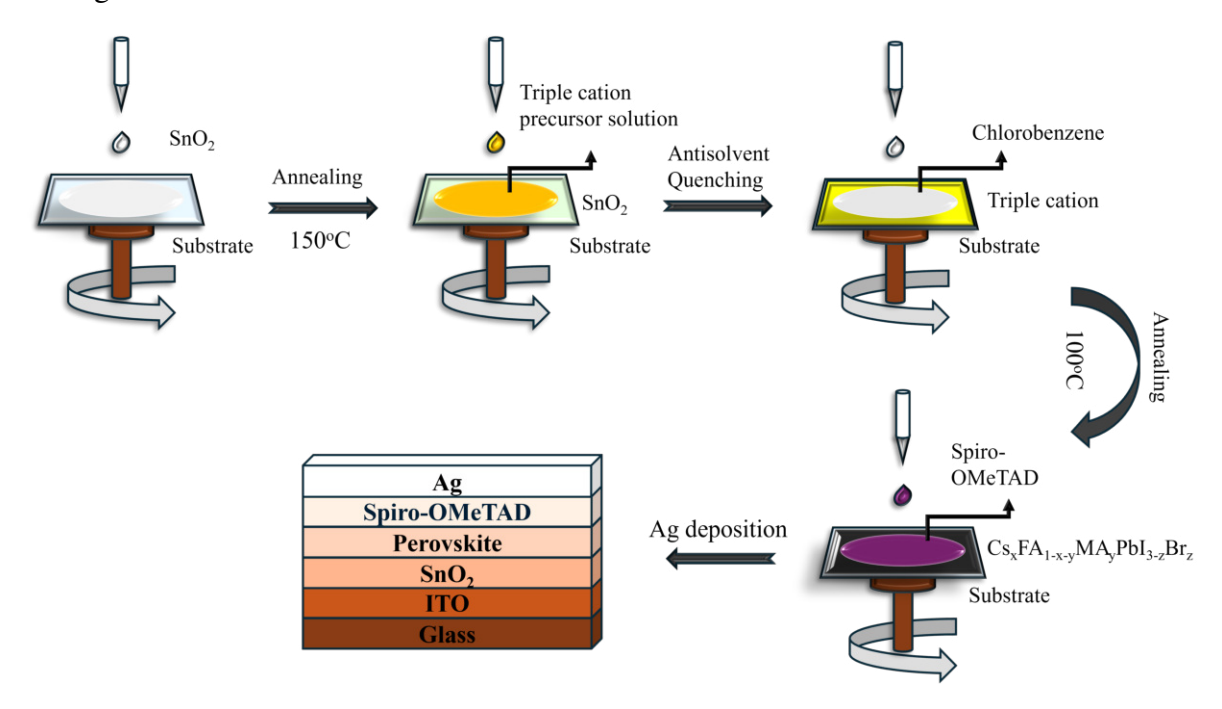


Figure 3.3: Schematic diagram of Spin Coating and Antisolvent quenching

After the spin coating process, silver (Ag) was deposited, which is the positive electrode of the device.

### 3.2 Experimental Work Stage 1:

At first, we tried to make PD in lateral configuration with the active layer of  $\alpha$ -FA<sub>1-x</sub>MA<sub>x</sub>PbI<sub>3</sub> by spin coating method. The lateral configuration is very easy to fabricate PDs specially for students who are experiencing solution-processable fabrication for the first time. It needs fewer steps, and no need to provide ETL, HTL layers and deposit a different electrode. However, the fabrication process is slightly different from the nip architecture. We make a channel of a few millimeters by etching the layer of ITO, then we follow the same steps of cleaning, and then fabricate  $\alpha$ -FA<sub>1-x</sub>MA<sub>x</sub>PbI<sub>3</sub> perovskite by 2-step spin coating (Fig. 3.4).

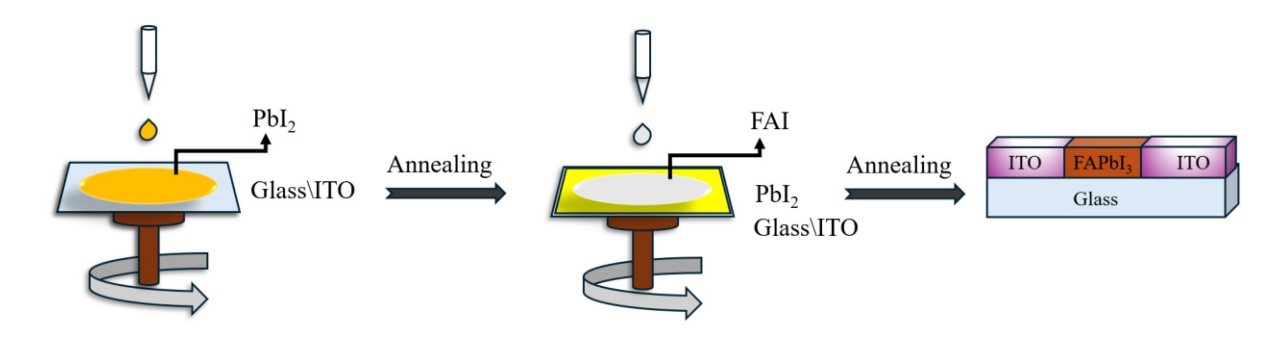


Figure 3.4: Spin Coating process for Lateral Configuration

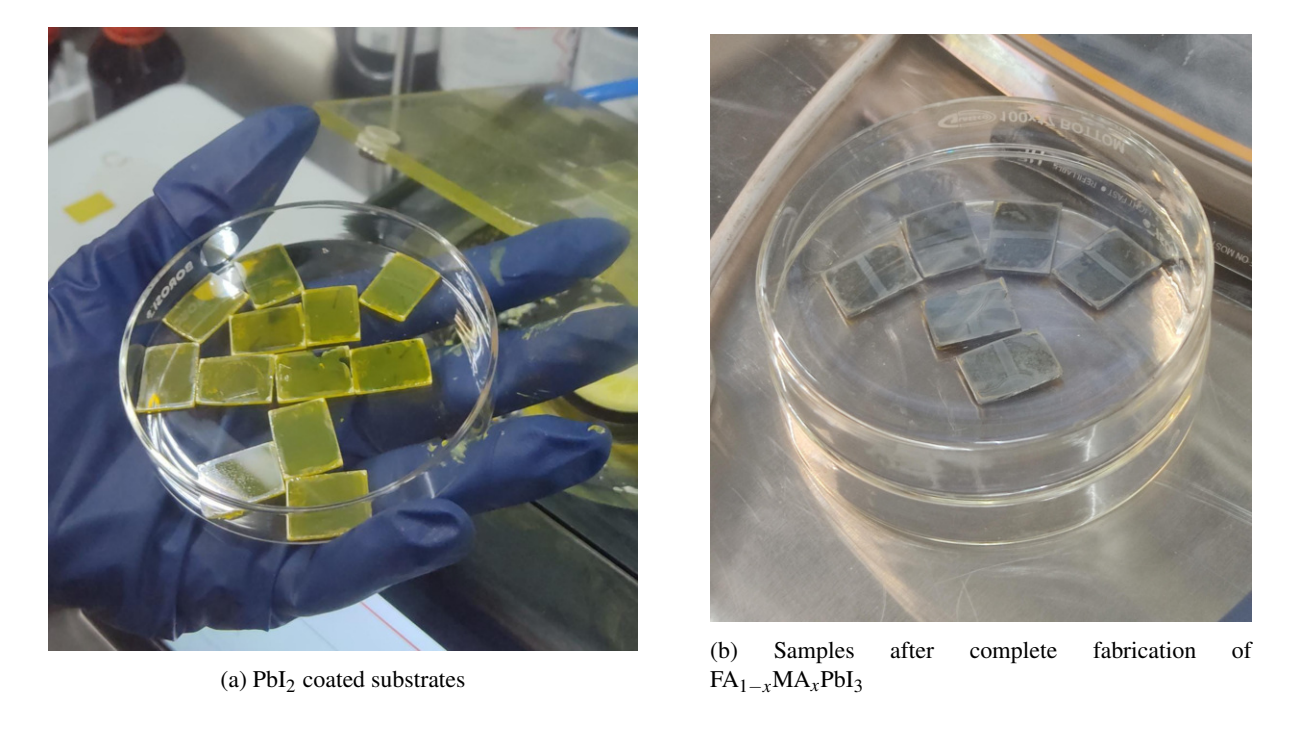


Figure 3.5: Snapshots taken during the process

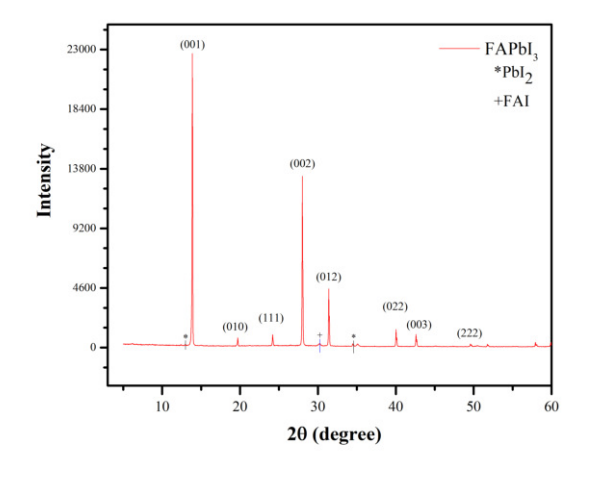
#### 3.2.1 Characterization & Results and Discussion

After successfully preparing the sample, we performed SEM and XRD material characterization. For optoelectronic characterization, we use Osiila solar simulator (for producing various monochromatic light), Osiila source measurement unit (SMUs), and Keithley 2450 source-meter. All optoelectronic measurements were performed in a completely dark box.

#### **XRD:**

It can be seen in the XRD pattern of this sample that it was crystallized into the  $\alpha$ -phase of FAPbI<sub>3</sub> perfectly, with a very little impurity of PbI<sub>2</sub>. There are two most intense peaks at 13.85° and 27.98° with the Miller indices (001) and (002). This shows that **crystal growth** 

**is mainly along 001 family of planes**. This is also verified by previously reported data[15]. Crystal unit cell parameters were also calculated by using this pattern (Fig. 3.6b).



(a) XRD pattern obtained from the sample

Angle (θ)	Sin <sup>2</sup> 0	$\left  \frac{\sin^2 \theta}{\sin^2 \theta} \right _{\min}$	(h k l)
6.926	0.014541	1.000021	(0 0 1)
9.859	0.029318	2.016209	$(0\ 1\ 1)$
12.083	0.043818	3.013438	$(1 \ 1 \ 1)$
13.989	0.058436	4.018713	$(0\ 0\ 2)$
15.712	0.073334	5.04324	(0 1 2)
17.3745	0.089172	6.132423	$(1 \ 1 \ 2)$
20.038	0.117404	8.074027	$(0\ 2\ 2)$
21.2965	0.13191	9.071598	$(0\ 0\ 3)$
24.779	0.175661	12.08039	(2 2 2)
25.891	0.190672	13.11274	(023)
28.97	0.234596	16.13345	$(0\ 0\ 4)$

(b) Observed XRD pattern from the sample

Figure 3.6: XRD data of the sample

#### SEM:

We took SEM images of the sample at different magnifications to physically see the crystals and quality of the film. The grain size is also an important factor, which is directly related to resistivity and capacitance of the device. The grain size was also calculated by SEM images, which shows an average grain size of 1.3373  $\mu$ m. The uniform distribution and weight percentage of the atoms can be seen by Back Scattered Electrons (BSEs) and Energy Dispersive Spectroscopy, respectively (Fig. 3.9).

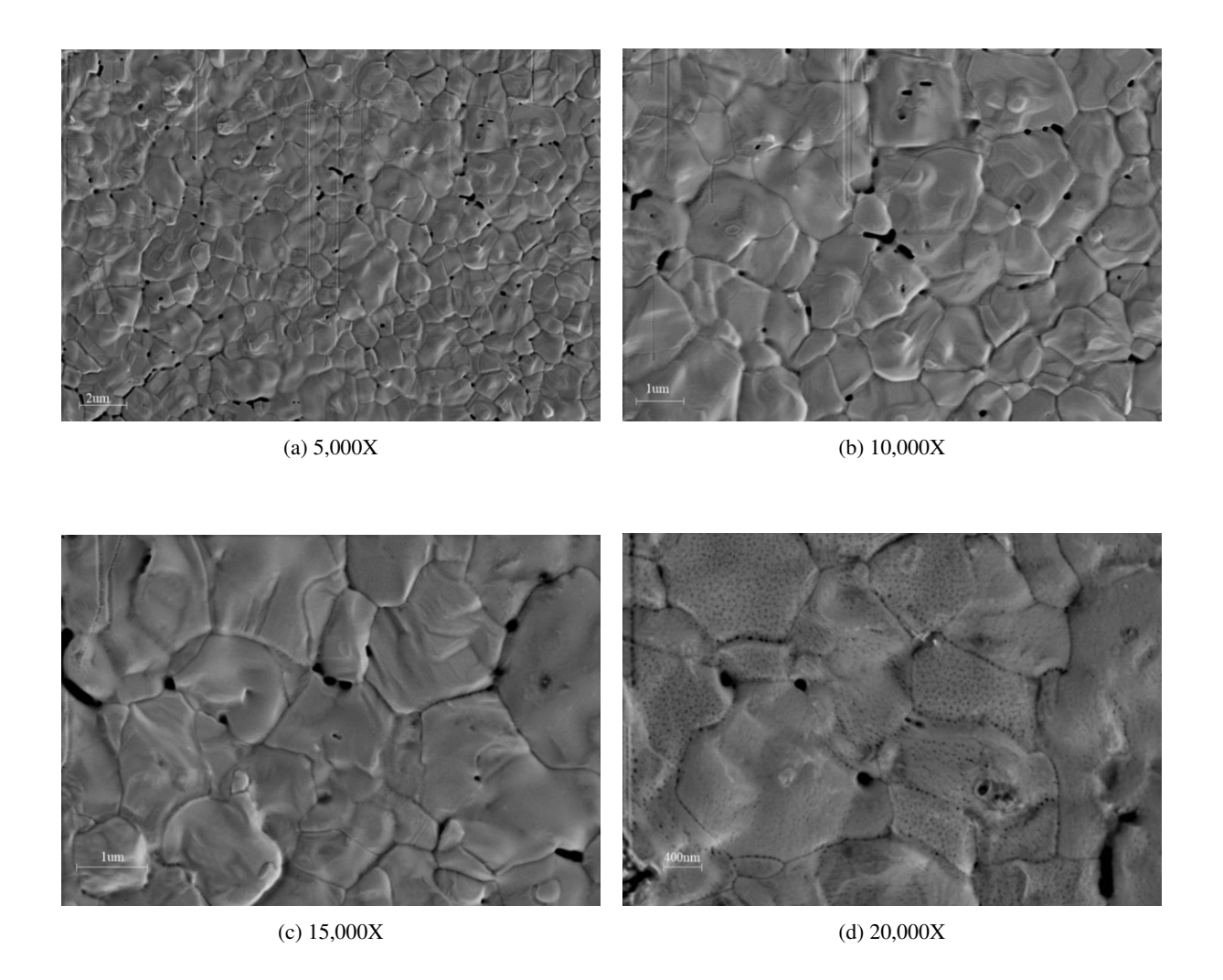


Figure 3.7: SEM images of  $FAPbI_3$  surface with different magnifications

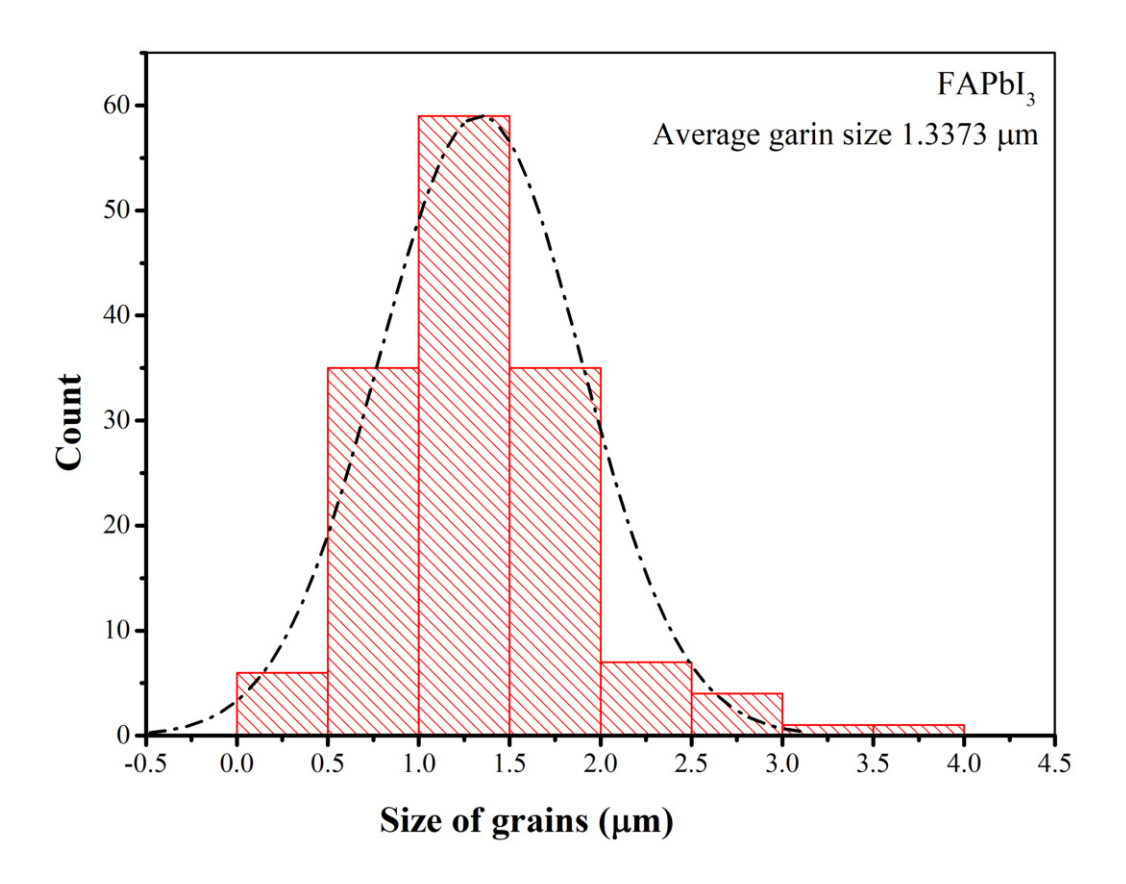
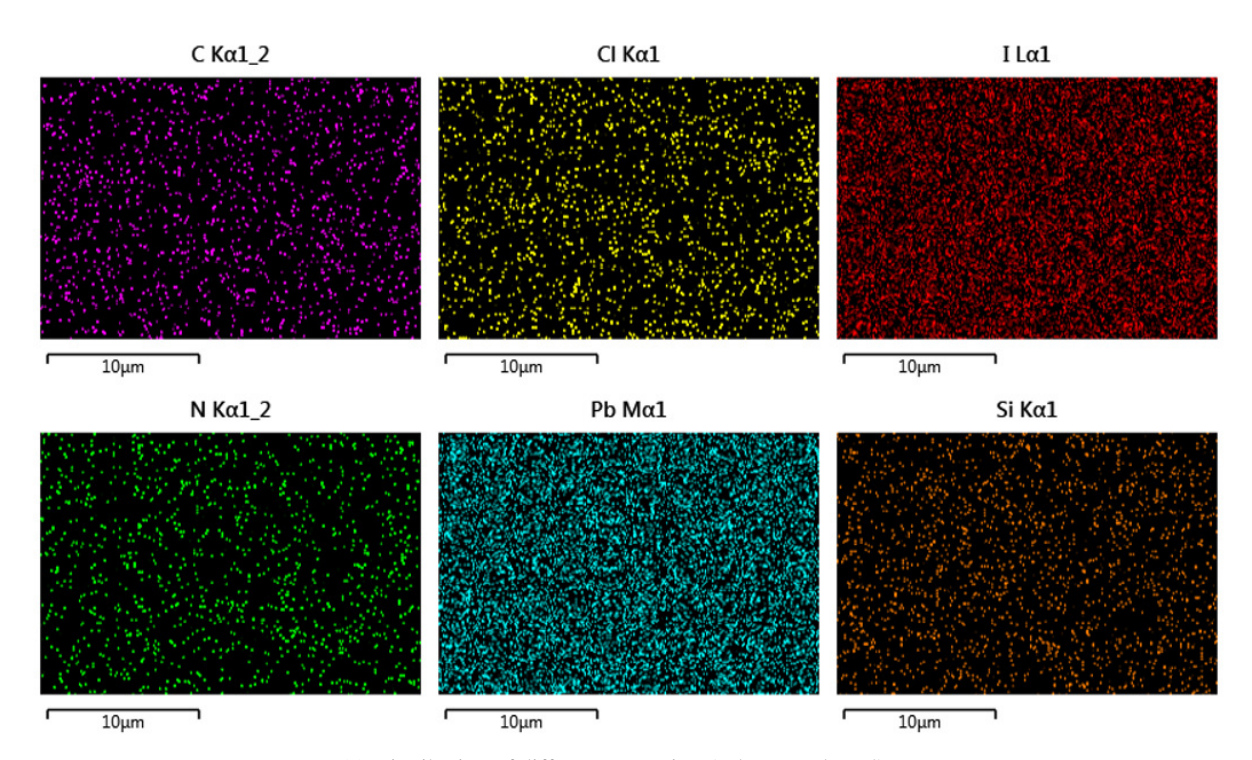
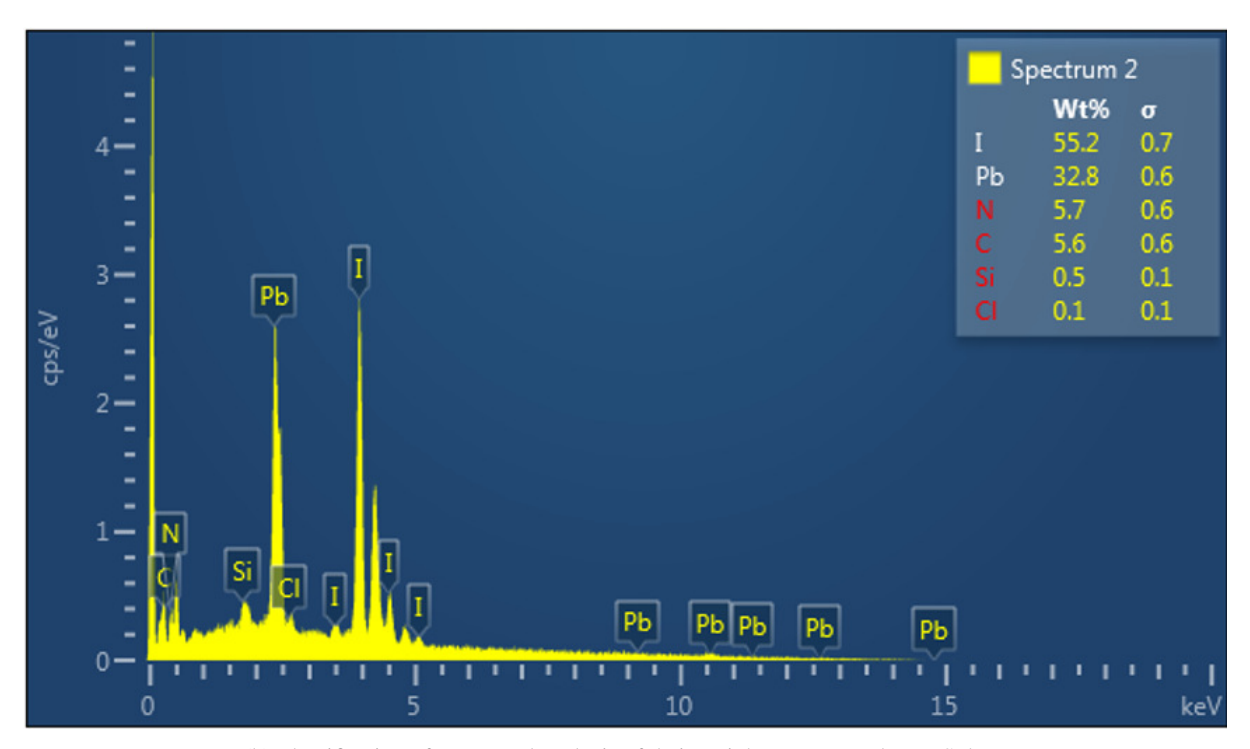


Figure 3.8: Grain size distribution of FAPbI<sub>3</sub> crystal



(a) Distribution of different atoms in FAPbI<sub>3</sub> seen by BSEs.



(b) Identification of atoms and analysis of their weight percentage by EDS data.

Figure 3.9: BSE and EDS data of FAPbI<sub>3</sub>

#### **UV-Visible DRS:**

We can easily calculate bandgap from UV-Vis spectroscopy, for our sample it is **1.49** eV.

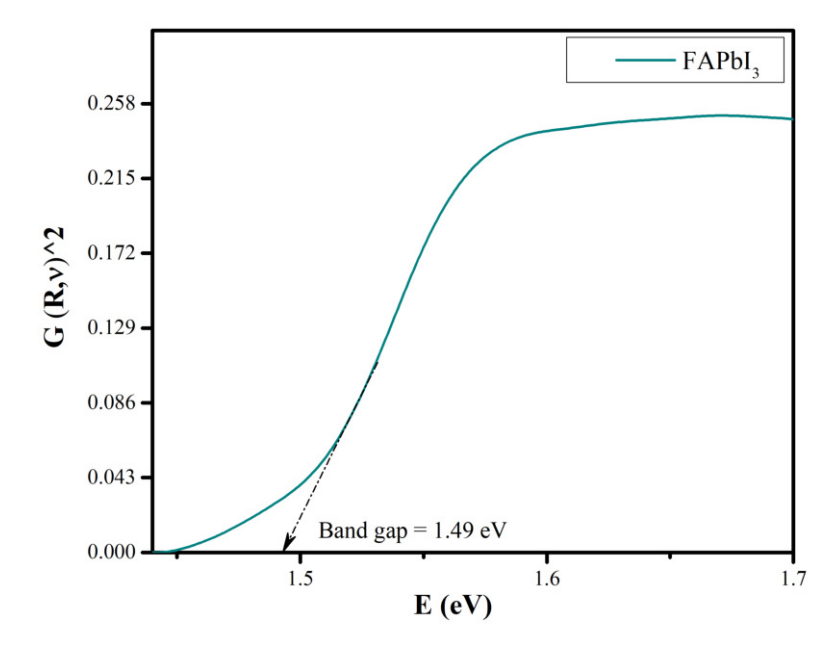
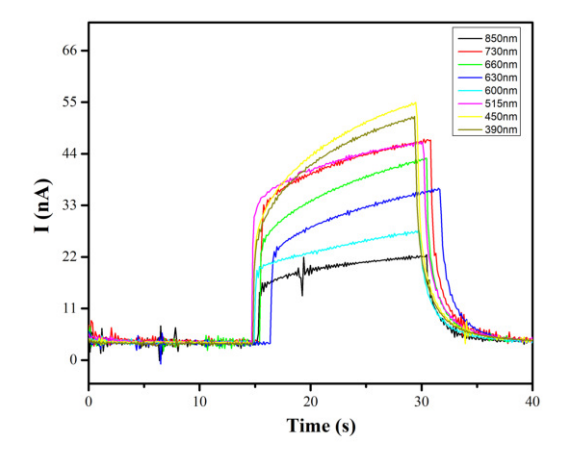


Figure 3.10: Bandgap of FAPbI<sub>3</sub> calculated from UV-Vis DRS data

#### **Response time:**

Response time is key parameter of PD which describes the radiation detection speed of PD. When the radiation falls on PD, it starts generating a photocurrent. But there is a time gap between radiation fall on its surface and detection of photocurrent, it should be 0 ideally. Similar happens when the light is turned off, the photocurrent takes few micro-seconds to vanish. The photo response time was calculated at different wavelengths (Fig. 3.11).



Wavelength (nm)	Rise Time (sec)	Fall Time (sec)
850	0.35	3.866
730	0.4	2.39
660	0.11	3.253
630	0.33	3.102
600	0.24	3.634
515	0.22	3.892
450	0.62	3.208
390	0.36	3.253

- (a) Response time of synthesized PD under luminescence with different wavelengths
- (b) Calculated Rise time and Fall time for different wavelengths

Figure 3.11: Photo response of the device at different wavelengths

#### **Responsivity:**

We recorded photo response of the PD at different wavelengths and calculated the responsivity. It can be seen from the Fig. 3.12 that **PD shows higher responsivity for 600nm wavelength**.

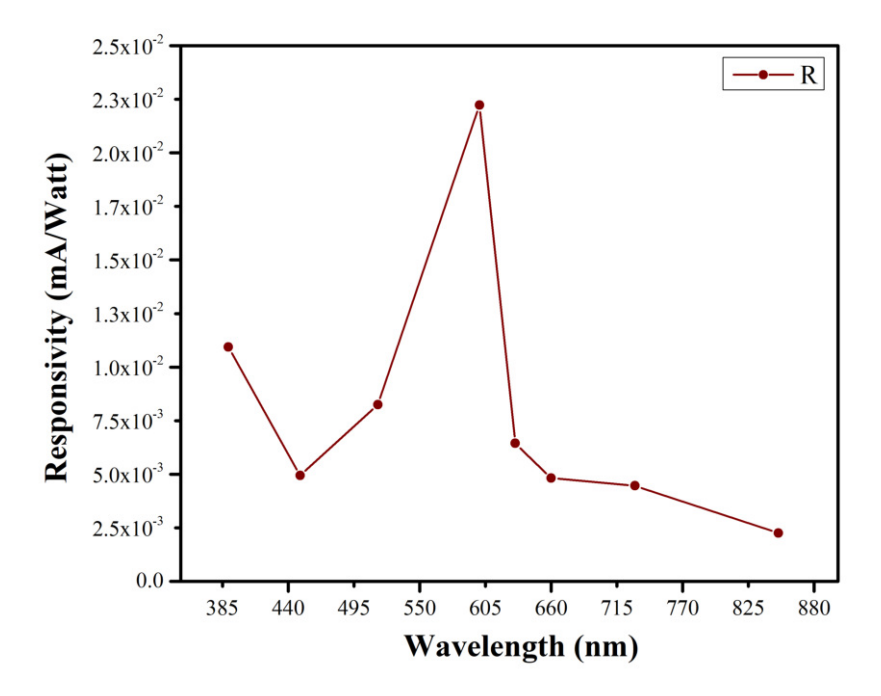


Figure 3.12: Responsivity of the device

#### EQE%:

EQE was calculated as described in section 1.4.2. PD has shown higher EQE at 600nm wavelength (Fig 3.13).

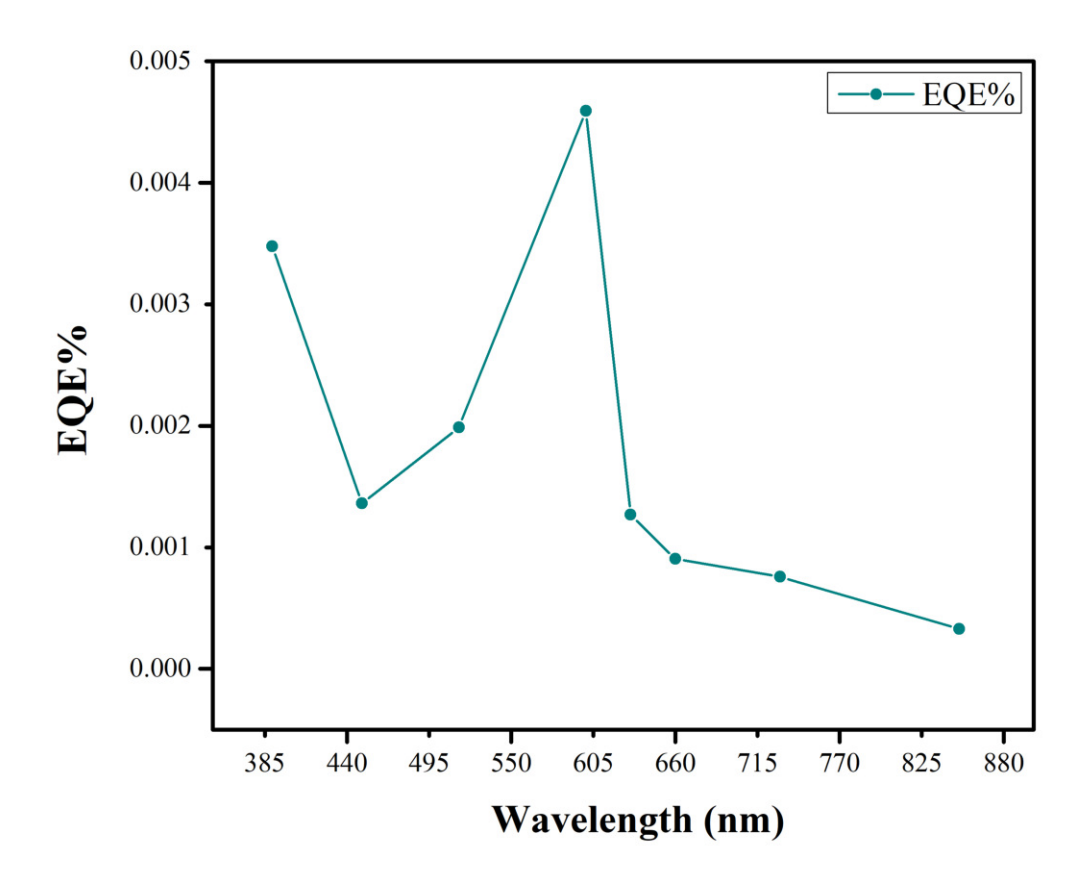


Figure 3.13: External coulombic efficiency of the device

## **Specific Detectivity:**

The Specific Detectivity (D\*) of this PD lies in the range of  $10^6$  Jones. The detectivity peaks at 600nm wavelength (Fig 3.14).

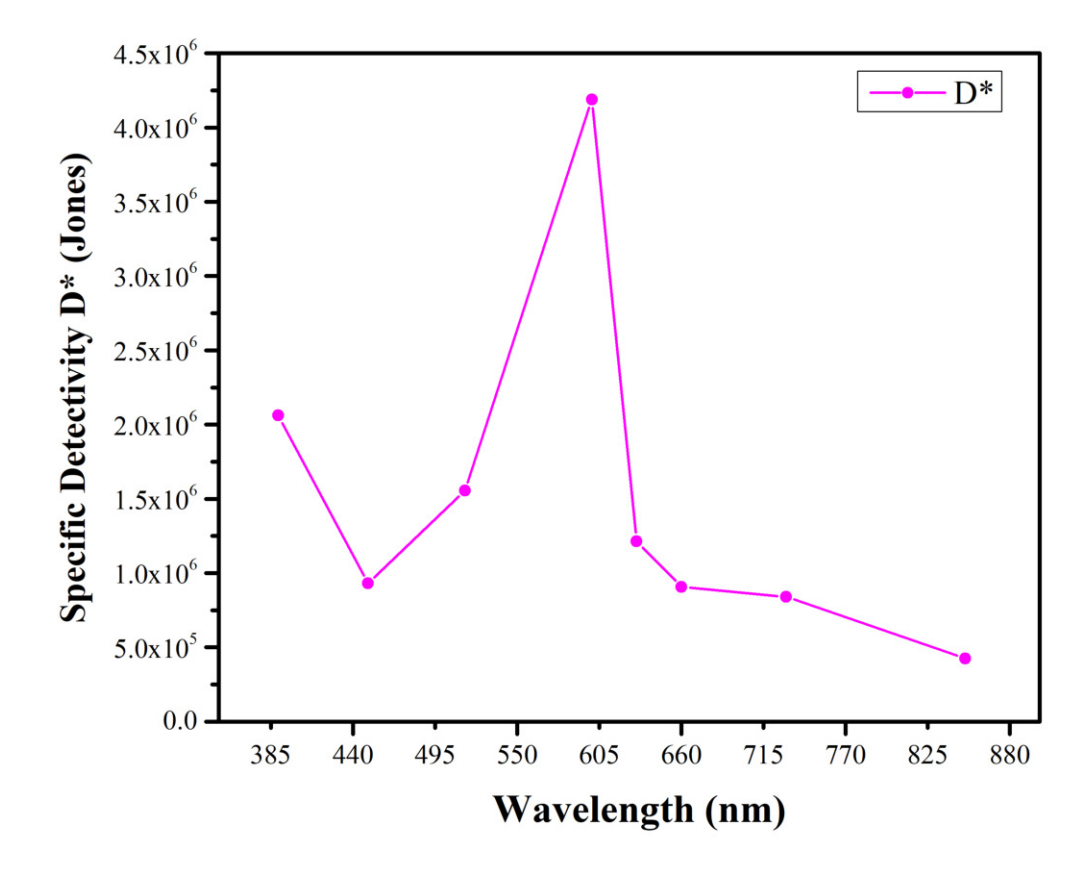


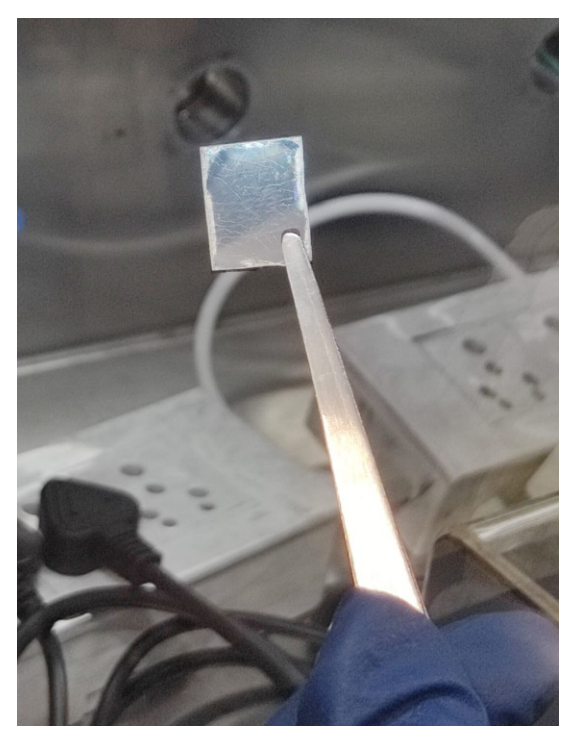
Figure 3.14: Specific Detectivity of the device D\*

However, lateral configuration is very easy to fabricate, and it shows significant photo response and photocurrent. However, it was observed that the rise and fall time is sufficiently large, lower responsivity, and very less EQE%. The etched channel that we make, which is also the active area of the device, is a few mm long. As we know that perovskites have diffusion lengths in the range of  $\mu$ m, many of the generated charge carries recombines before reaching at the electrodes. Even, it is hard to make a channel of some  $\mu$ m. These might be some reasons for the lower performance of the lateral device. In the upcoming sections, we will device improvement by doing fabrication in NIP-structure.

## 3.3 Experiment Stage 2

Previous photodetector (PD) was build in lateral configuration, which works as a photoconductor. This time we are fabricating PD in nip-configuration, which works as a photodiode. Also, this time we are trying triple cation  $Cs_xFA_{(1-x-y)}MA_yPbI_{3-z}Br_z$  composition, which lowers the formation energy of pristine FAPbI<sub>3</sub> and helps in the stabilization of it at room temperature[16, 17, 18]. This is evident that this composition of perovskite demonstrate enhanced properties in PD and solar cells. Moreover, this composition shows suitable bandgap which is main interest of us for the detection in the NIR region. Using this architecture and triple cation composition, we reported some positive enhancement in the properties of PD.

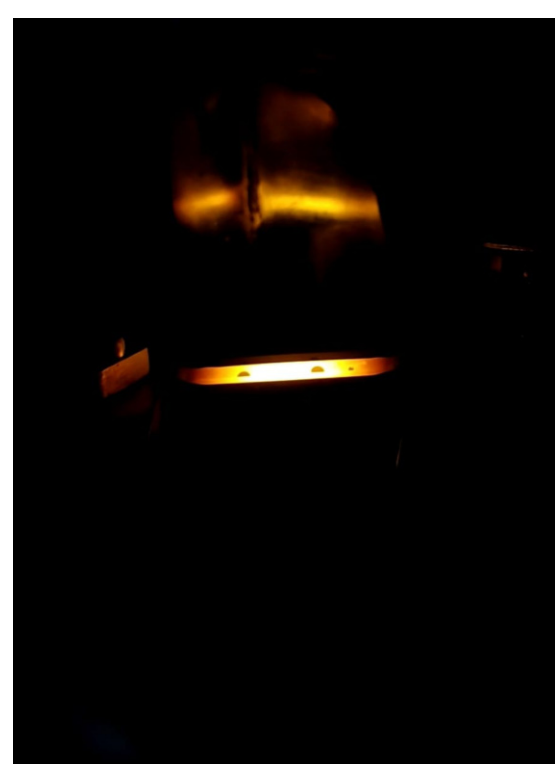
In order to optimize processing steps and other factors of fabrication, before we move to flexible substrate i.e. PET/ITO. The reason of choosing this particular composition beacuse we need to provide lesser temperature due to its lower formation energy. This speciality would help us when we would be making device on PET/ITO. This composition was fabricated by the anti solvent quenching method (described in Section 3.1.3). Since, the crystallization process is pretty fast during this quenching, the material feels stress and strain and this reflects into the cracks (Fig. 3.15). Triple cation composition film is very shiny for having smaller grain size.



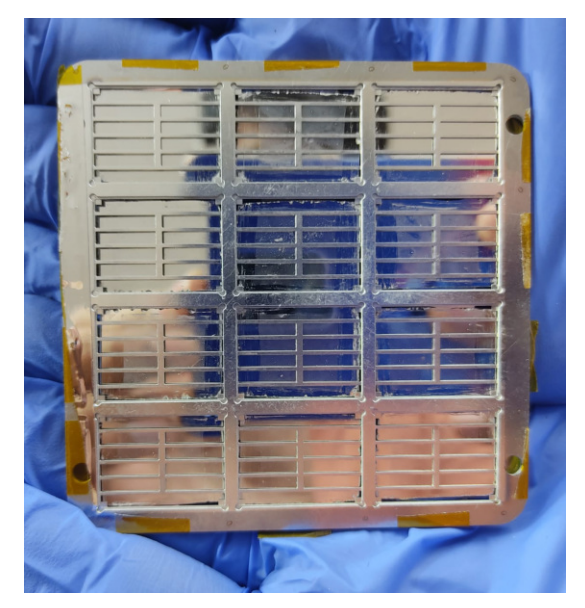
(a) Cracks observed during after anti solvent quenching



(b) Shiny film of triple cation composition



(c) Samples placed inside the thermal evaporator for Ag deposition



(d) Final device after all the process done

Figure 3.15: Snapshots taken during the device fabrication of triple cation composition

#### 3.3.1 Characterization & Results and Discussion

Same techniques and instruments, which are described in section 2.2.1 were used this time as well.

#### XRD:

The XRD pattern of the sample is demonstrated in the Fig. 3.16, which agrees well with previously available XRD data of the triple cation composition[16]. Thus, XRD data confirm that this composition is useful for keeping FAPbI<sub>3</sub> in its photoactive  $\alpha$  phase at room temperature. Used X-rays are having wavelength same as 1.51Å.

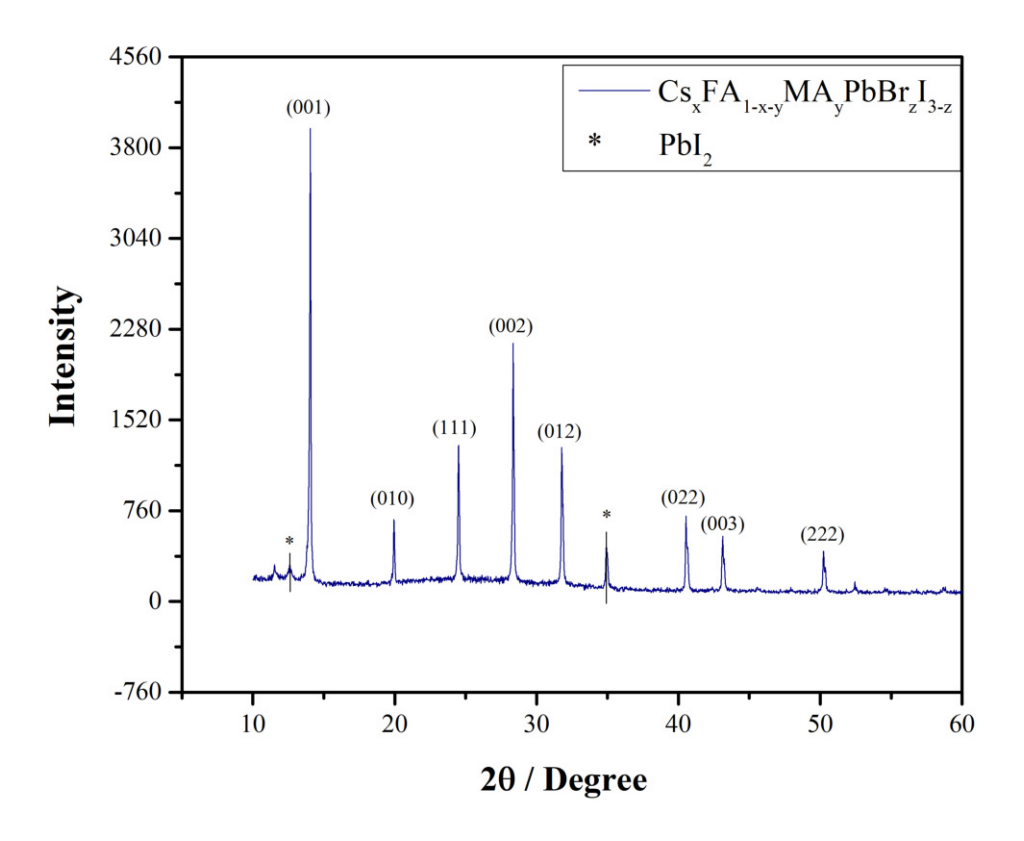


Figure 3.16: XRD pattern of  $Cs_xFA_{(1-x-y)}MA_yPbI_{3-z}Br_z$ 

#### **UV-Visible Spectroscopy:**

For this triple cation composition, we calculated bandgap by using UV-Vis spectroscopy that came out 1.467 eV (Fig. 3.17). **This is comparable to 845.26 nm (NIR) energy radiation** and photon with this much energy that generate electron-hole pair. Thus doping of Cs lowers the bandgap of pristine FAPbI<sub>3</sub>.

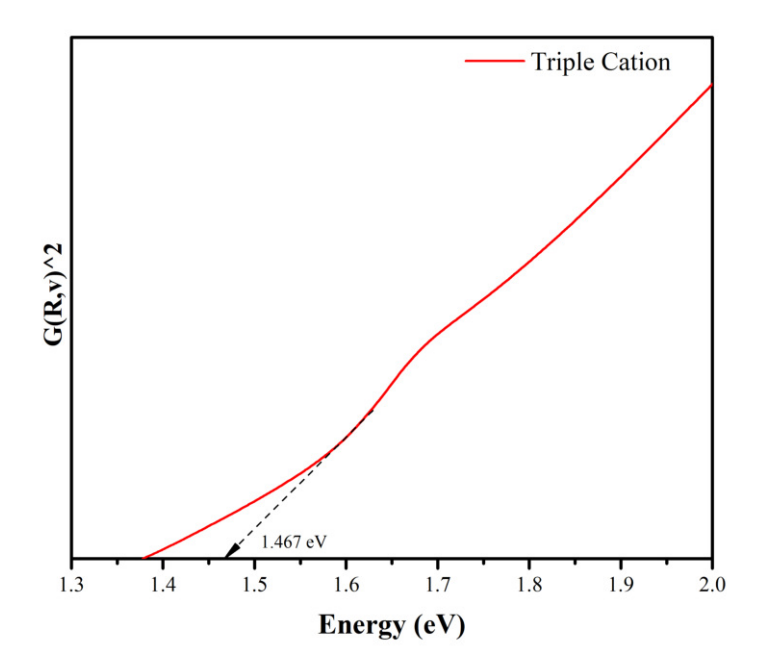


Figure 3.17: Bandgap of triple cation calculated from UV-Vis data

#### SEM:

SEM images clearly show that average grain size (0.501  $\mu$ m, Fig. 3.19) of the triple cation composition is half of the pristine FAPbI<sub>3</sub>. This difference can be attributed to the rapid growth of nucleation centers during anti-solvent quenching and need to provide less energy for crystalization. So many nucleation centers result into smaller grain size of the crystal. Also, the triple cation film is very shiny because of small size of grains.

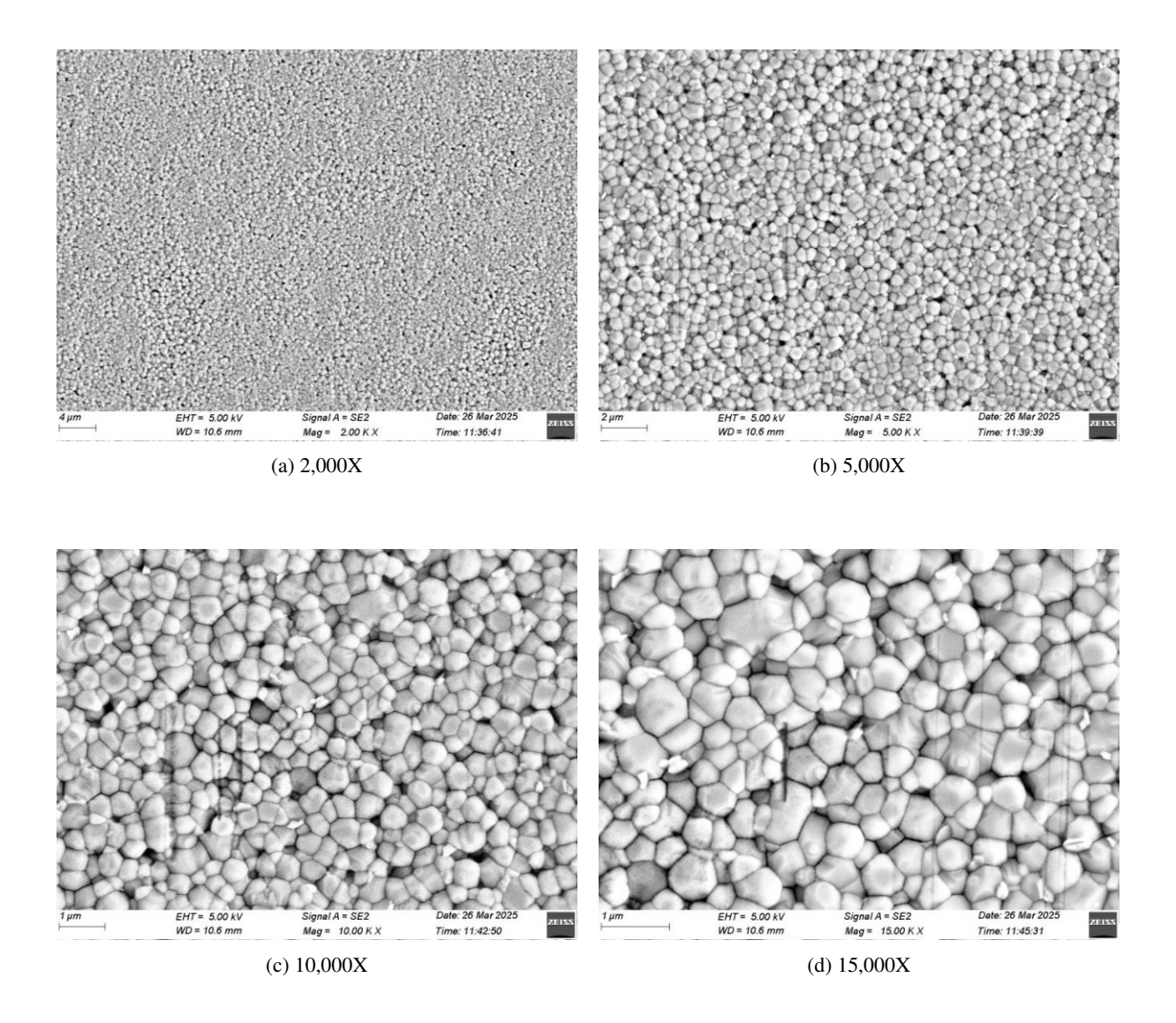


Figure 3.18: SEM images of  $Cs_xFA_{(1-x-y)}MA_yPbI_{3-z}Br_z$  surface with different magnifications

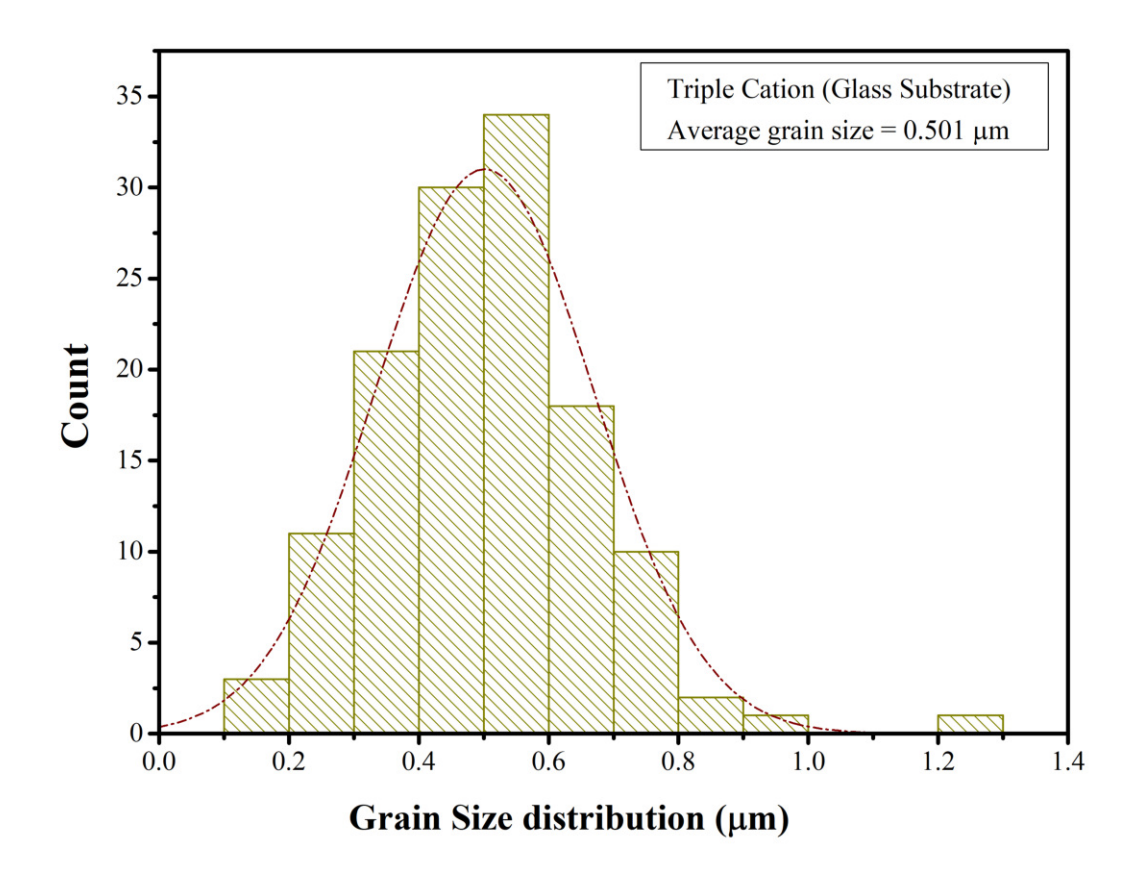


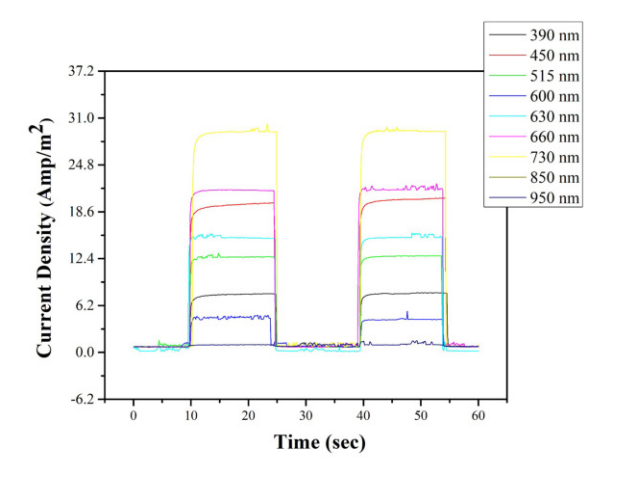
Figure 3.19: Grain size distribution of  $Cs_xFA_{(1-x-y)}MA_yPbI_{3-z}Br_z$  crystal

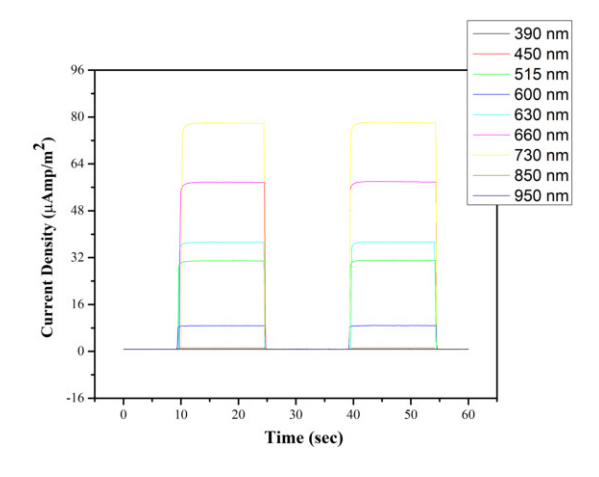
#### Rise time and Fall time:

We are providing data of best 2 samples that we fabricated. Corresponding response time of those 2 samples on the different wavelengths is presented in fig 2.16. The devices showed maximum photocurrent at 730nm wavelength, which is of our interest. So, we calculated rise time and fall time for both devices at 730nm and they are **280 ms** and **125 ms** respectively for device 1 and **109 ms** and **109 ms** respectively for device 2 (Fig. 3.20).

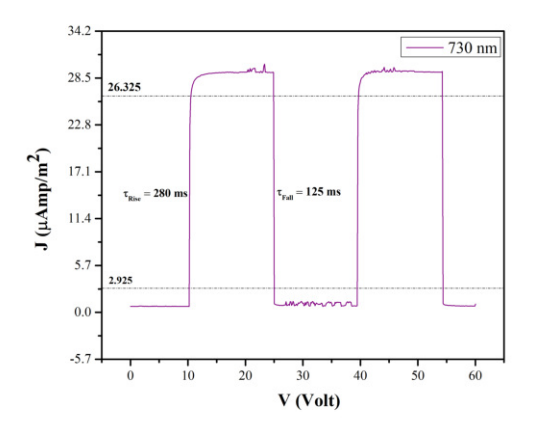
#### I-V Charactrization:

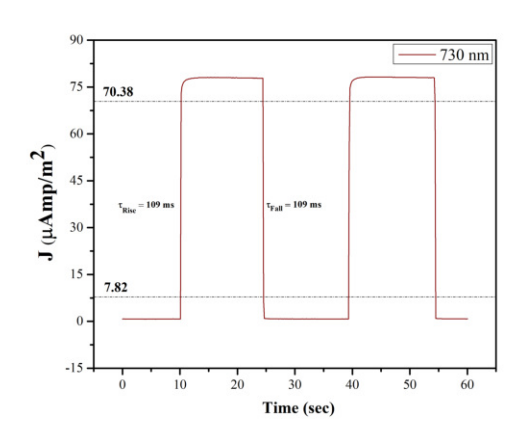
Photodetectors are used in reverse biased configuration in an electronic circuit. It is expected that a PD shows an increment in the output current when light of a suitable wavelength falls on its surface. The output current of a PD device in the presence of light is called photocurrent. We are showing the photocurrent response of those 2 samples in the presence of





- (a) Response time of device 1 at different wavelengths
- (b) Response time of device 2 at different wavelengths





- (c) Response time of device 1 at 730 nm wavelength
- (d) Response time of device 2 at 730 nm wavelength

Figure 3.20: Response time of  $Cs_xFA_{(1-x-y)}MA_yPbI_{3-z}Br_z$  PD (correction: J unit= $\mu$ Amp/cm<sup>2</sup>)

different wavelengths and in the dark mode as well. Photocurrent is recorded as a function of varying voltage in the range of -1 to 1 volts and it is clear from the Fig. 3.21 that this PD is able to provide significant  $V_{oc}$ . Therefore, the triple cation composition is a potential candidate for photovoltaics applications. It can be seen in the Fig. 3.21c that the photocurrent increases by 2 orders as the response of PD in the light. Moreover, PD gives a significant amount of photocurrent even when there is no external voltage is applied, which makes it able for self powered PD [20, 21].

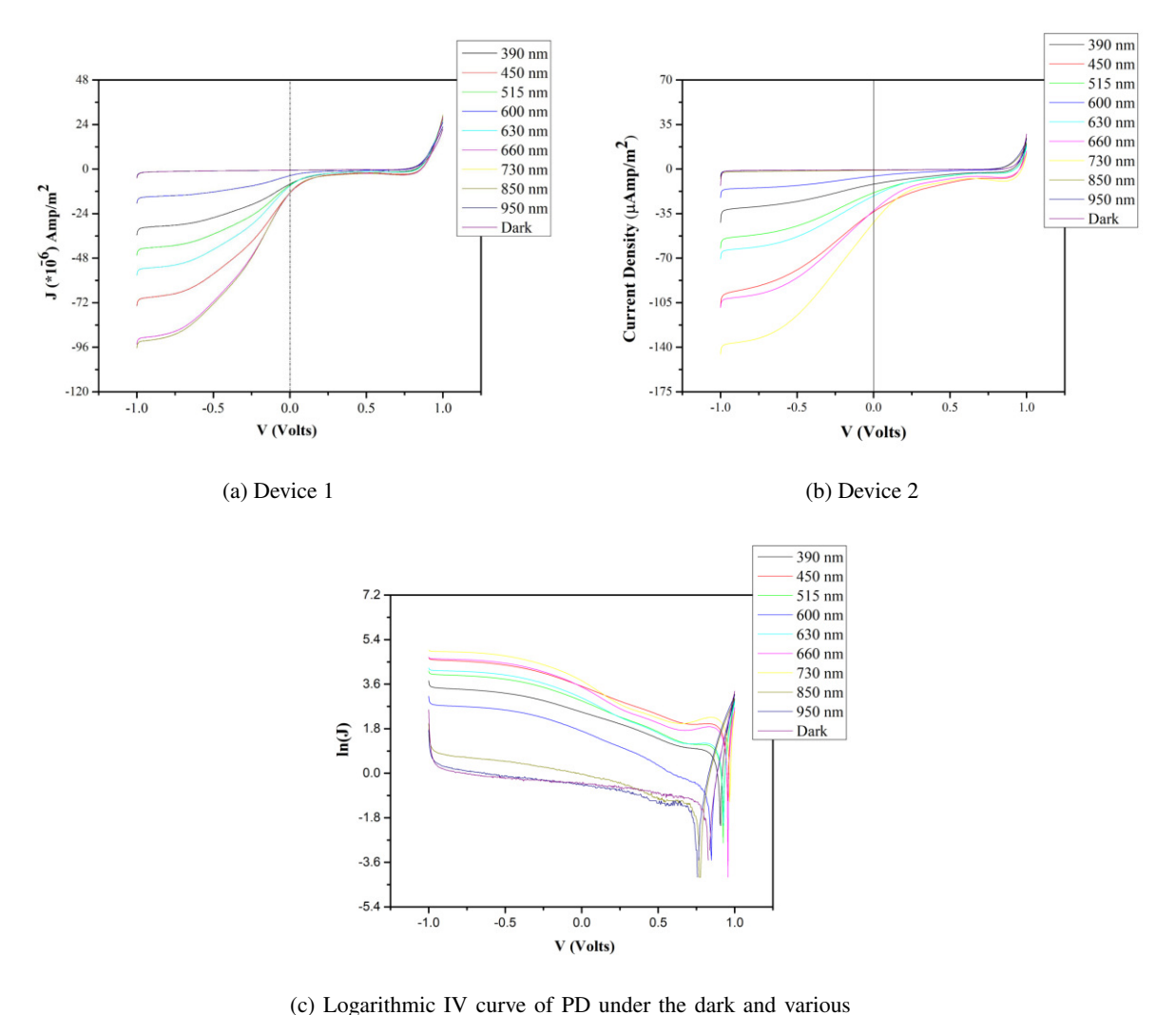


Figure 3.21: I-V characteristics of  $Cs_xFA_{(1-x-y)}MA_yPbI_{3-z}Br_z$  PD

monochromatic light

#### **Responsivity:**

Responsivity at different wavelengths is plotted in Fig. 3.22. The peak responsivity shifts to 730 nm wavelength light, if we compare with  $FA_{1-x}MA_xPbI_3$ , this result is supported

by Uv-Visible data plot.

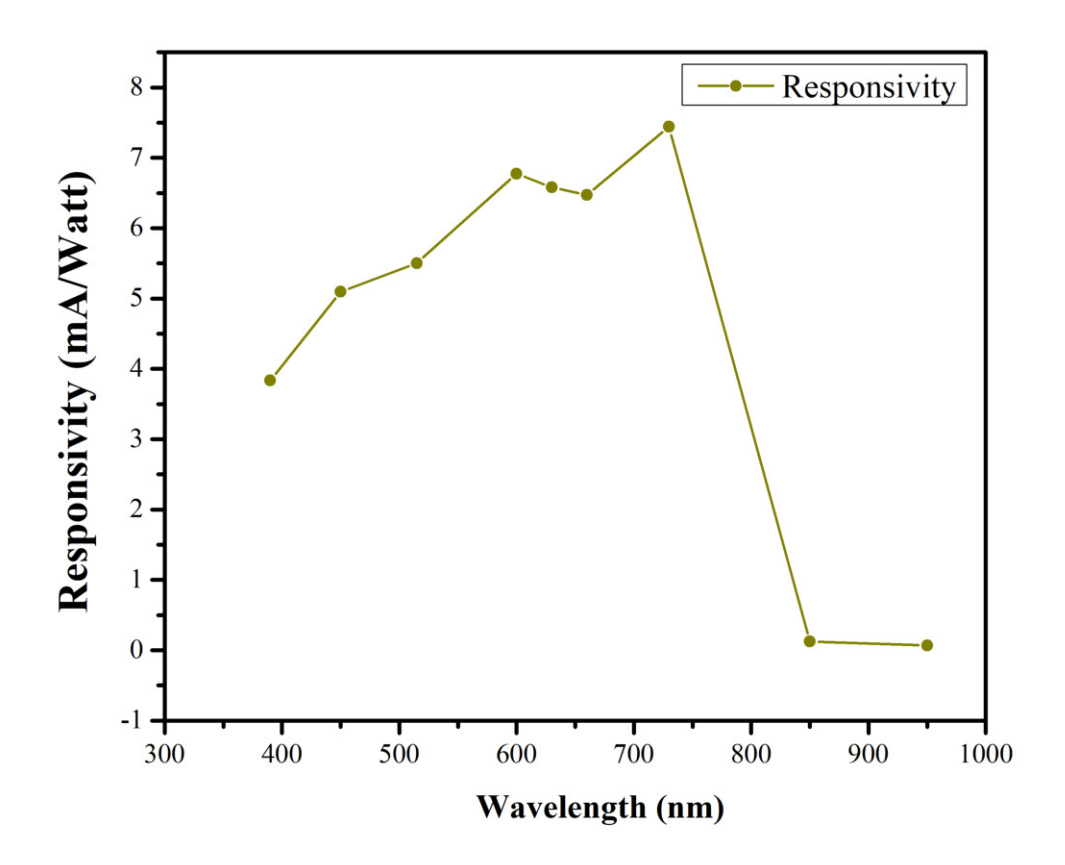


Figure 3.22: Responsivity of the device

## EQE%:

From Fig. 3.23, we can conclude that the PD has a good EQE for the range 400nm-730nm. It is better than the previously lateral configuration device.

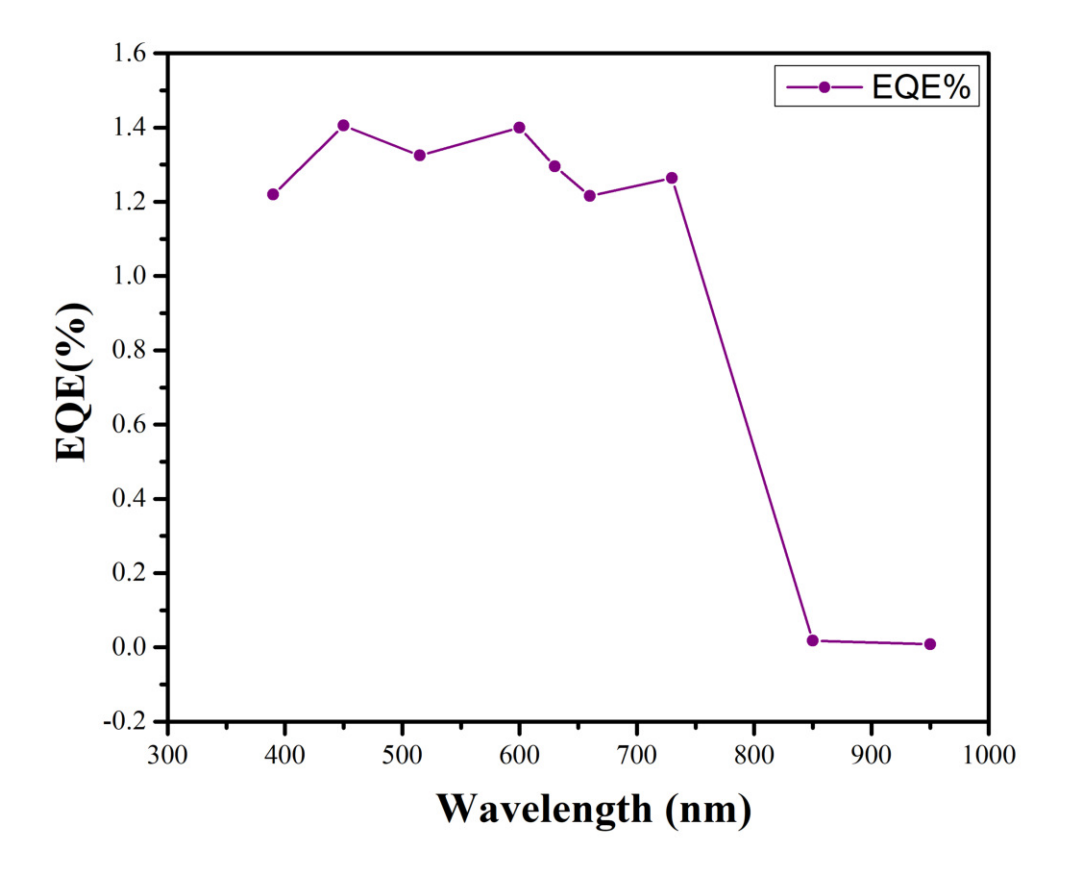


Figure 3.23: External coulombic efficiency of the  $Cs_xFA_{(1-x-y)}MA_yPbI_{3-z}Br_z$  device

#### **Specific Detectivity:**

The Specific Detectivity (D\*) of this PD is one order higher than the lateral configuration device, and it peaks at 730nm wavelength (Fig. 3.24).

The NIP-structure is much efficient than lateral one. Following the above results, NIP-structure shows better photocurrent (in the  $\mu$ Amp range), Responsivity, Specific Detectivity (D\*), EQE%, shorter rise time and fall time. Having achieved this, we have optimized the fabrication process and our next step to fabricate PD device on flexible PET/ITO.

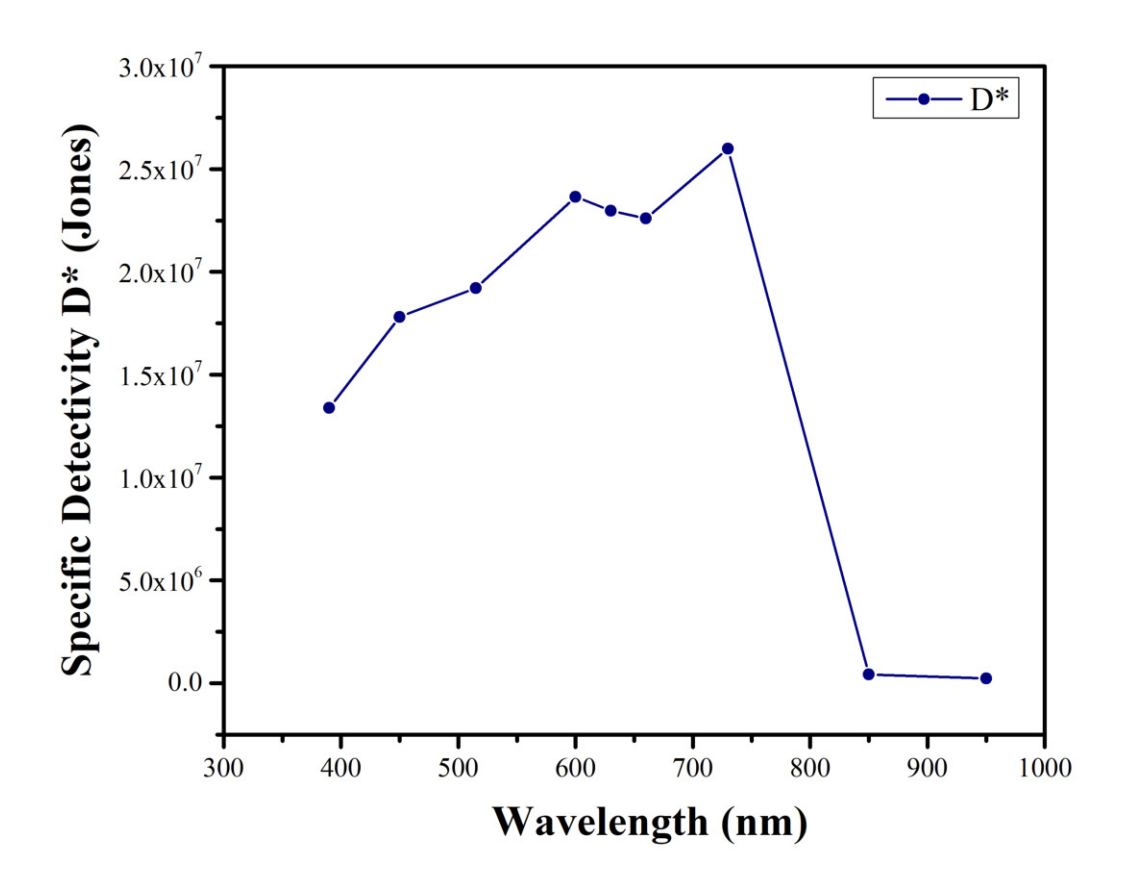


Figure 3.24: Specific Detectivity of the device D\*

# 3.4 Experimental Stage 3

This is the last stage and we will show our efforts to fabricate PD on flexible PET substrate. We failed to produce good quality PD in the initial tries but in the final trial we succeeded. This section is completely dedicated to the flexible PD and we will describe our 3 trials ahead.

### **3.4.1** Trial 1 (failed!) :

At frist, we tried to fabricate  $FA_{1-x}MA_xPbI_3$  composition on ITO coated PET. We kept the whole process the same except changing the chuck of spin coater. Typical chucks have a large hole for holding the substrate by vacuum. Since our substrate is flexible; a normal chuck may suppress it in the center, hence coating would not be uniform. Therefore, we made a new chuck with multiple small holes (Fig. 3.25) to distribute the elimination of this effect.



Figure 3.25: Chuck with multiple holes

#### 3.4.2 Characterization, Results & Discussion

Characterization methods and instruments are the same as described before.

#### XRD:

XRD pattern shows that the film of  $FA_{1-x}MA_xPbI_3$  is perfectly crystalline and in the  $\alpha$ -phase, it matches with perviously reported data.

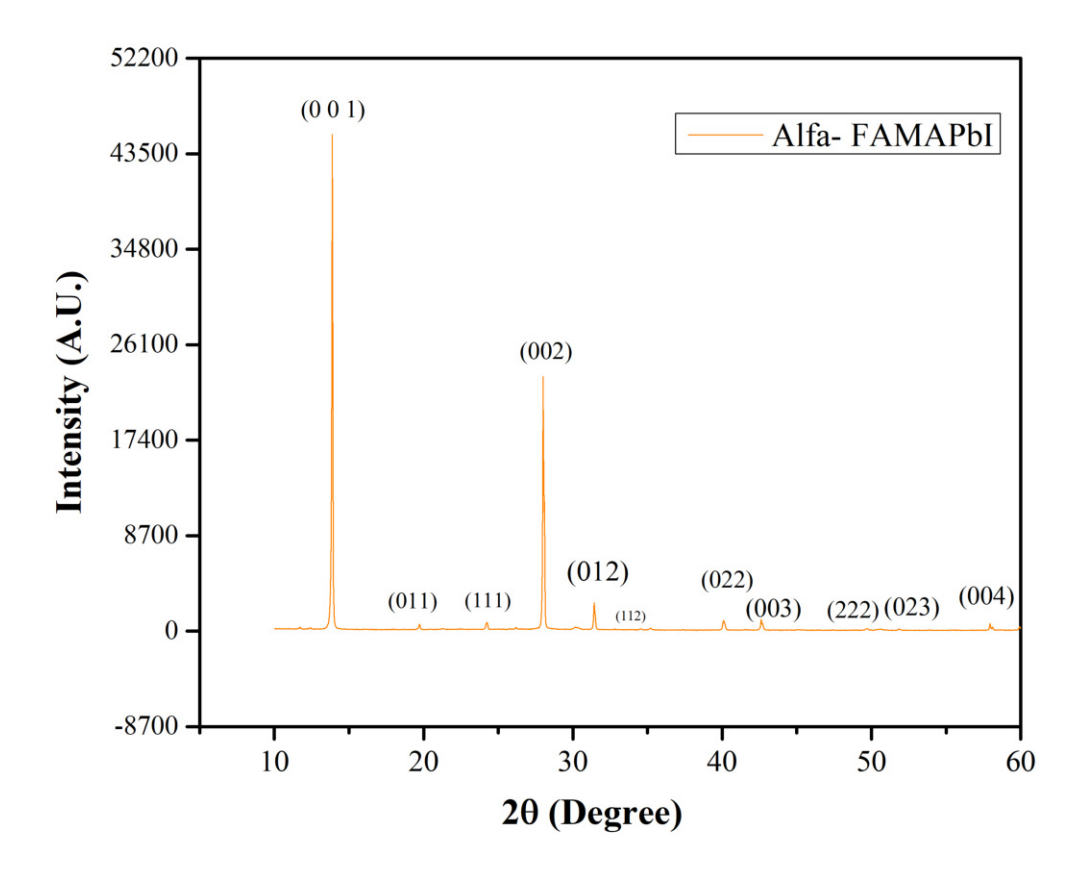


Figure 3.26: XRD pattern of FA<sub>1-x</sub>MA<sub>x</sub>PbI<sub>3</sub> coated on PET substrate

#### SEM:

SEM images shows that crystallization is not the problem, the film was fabricated so well on the PET substrate. The average grain size was found to be  $0.863_mum$ , the result is very similar to the coating of  $FA_{1-x}MA_xPbI_3$  on the glass substrate (Section 3.2.1). EDS and BSE plots are shown in Fig. 3.29.

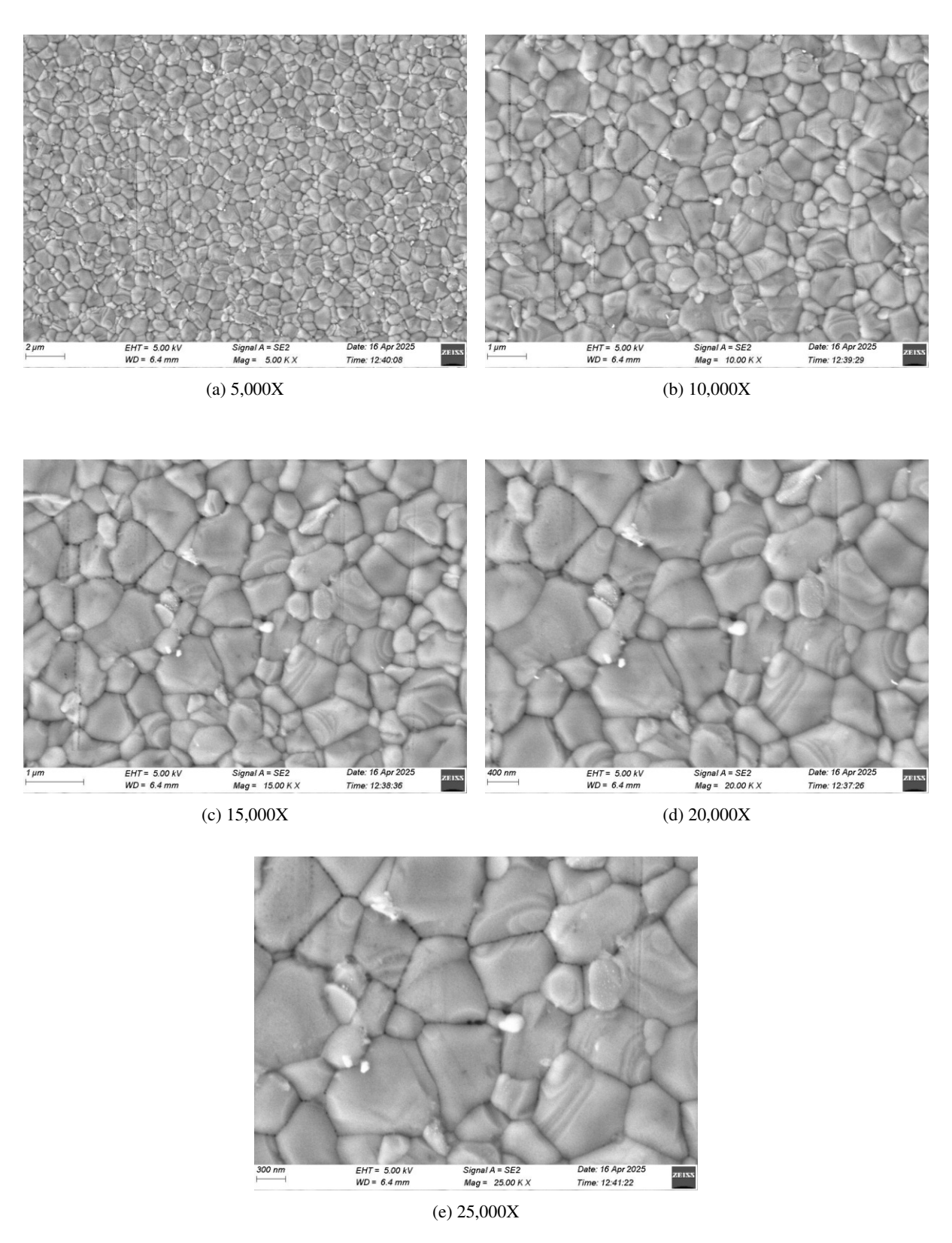


Figure 3.27: SEM images of  $FA_{1-x}MA_xPbI_3$  coated on PET substrate

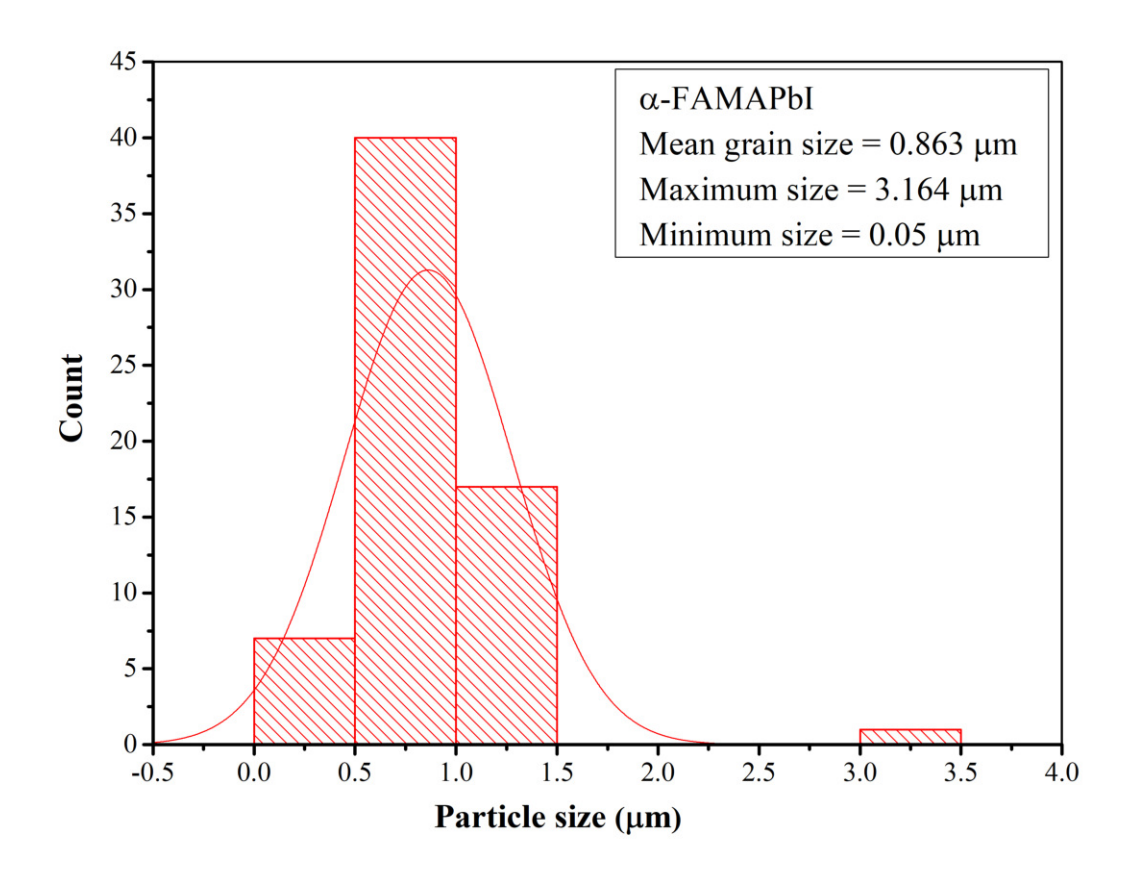
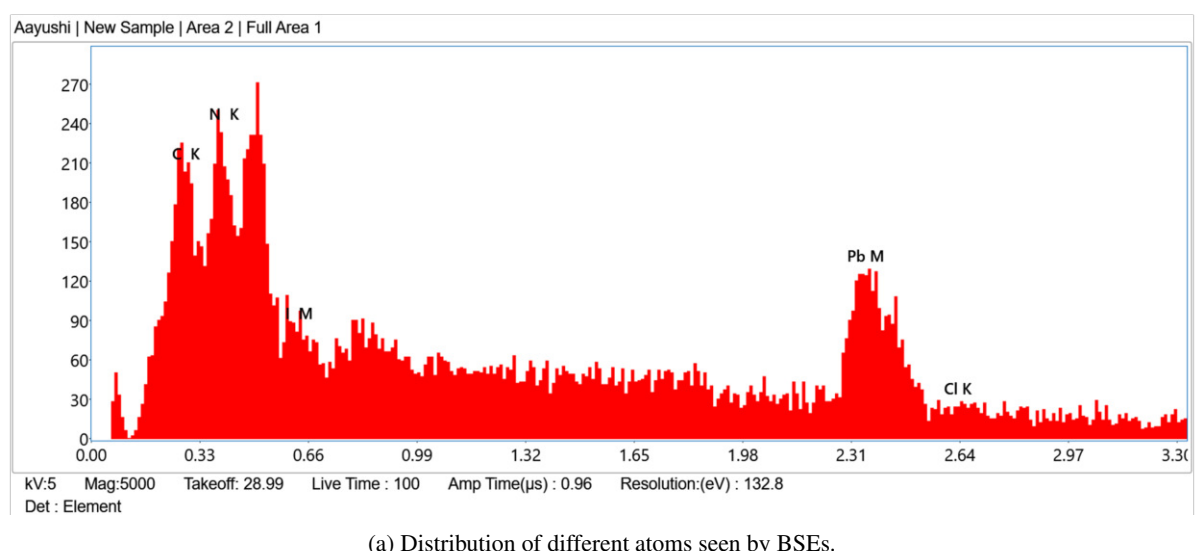
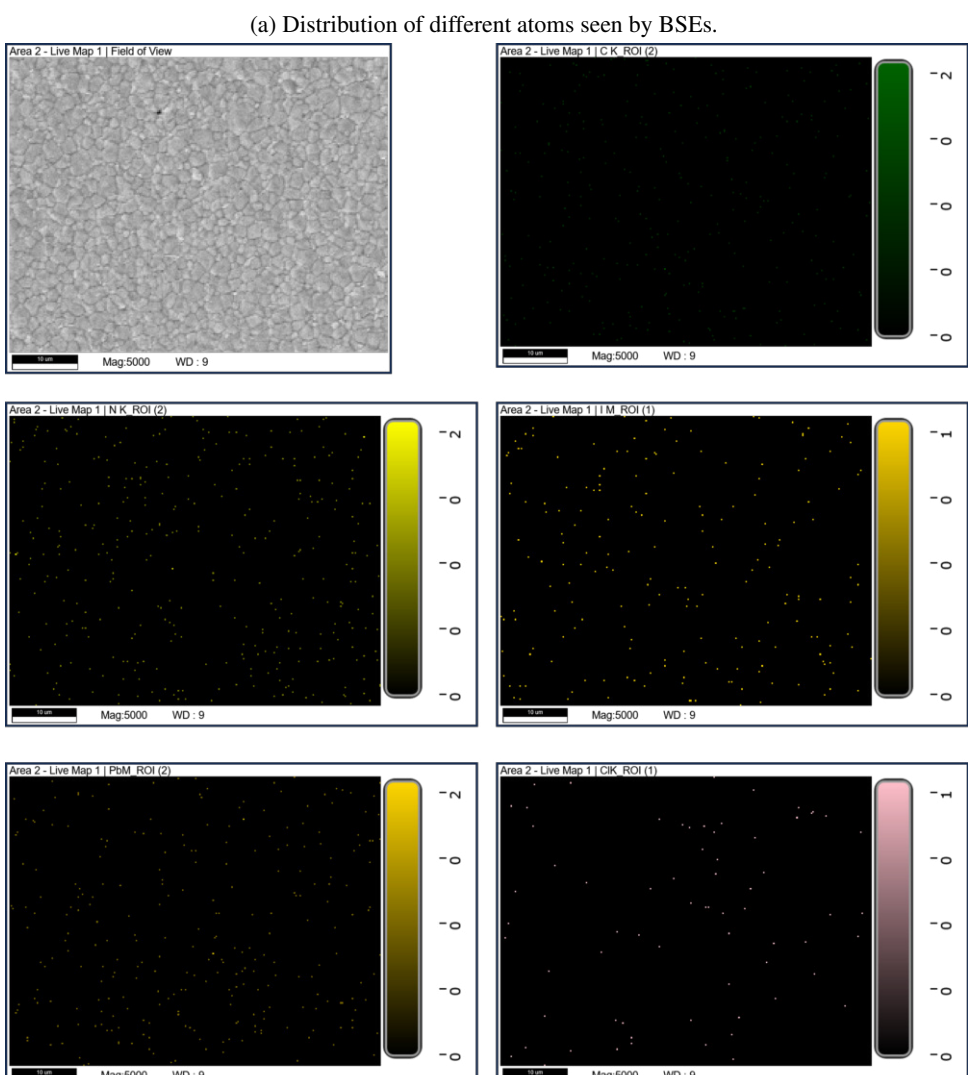


Figure 3.28: Grain size distribution of  $FA_{1-x}MA_xPbI_3$  (coated on PET)





(b) Identification of atoms and analysis of their weight percentage by EDS data.

Figure 3.29: BSE and EDS data of  $FA_{1-x}MA_xPbI_3$  (coated on PET)

#### **IV Characteristic:**

IV curve is shown in Fig. 3.30, and it can be clearly seen that either devices are shorted or do not behave properly. The graph is too noisy, we failed to get wanted results this time.

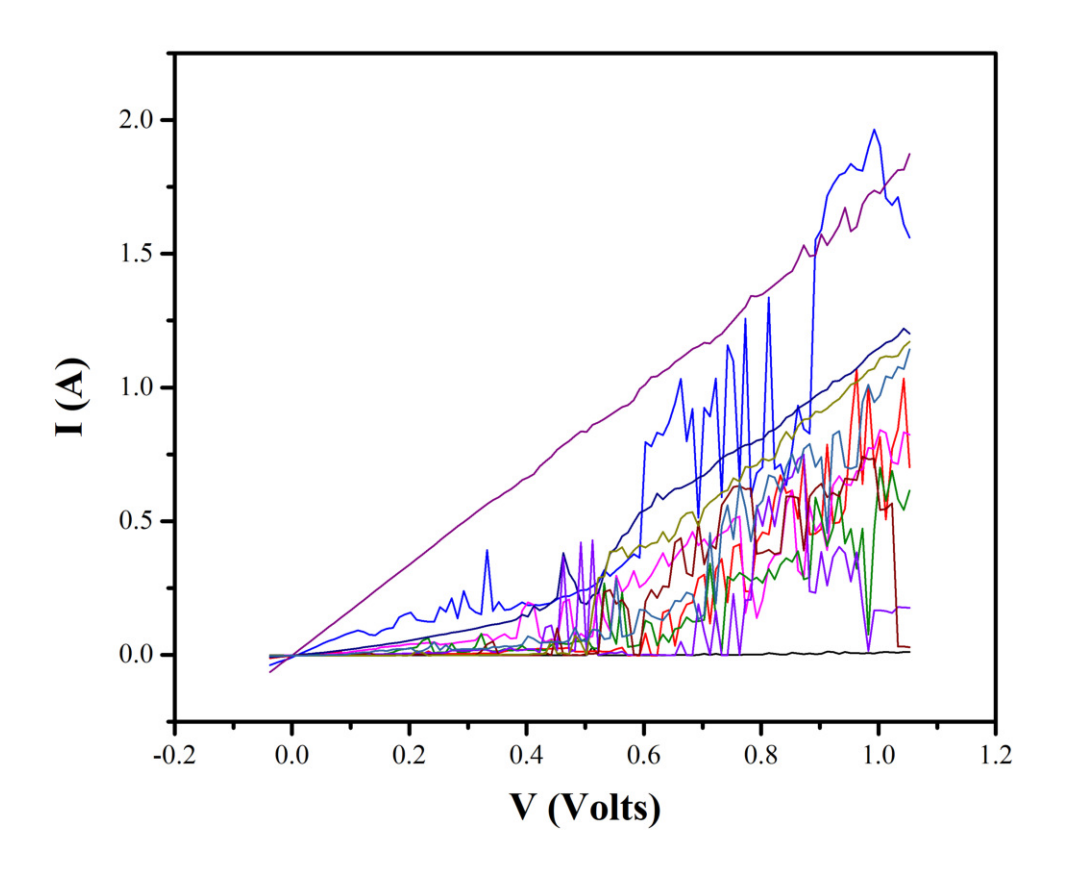


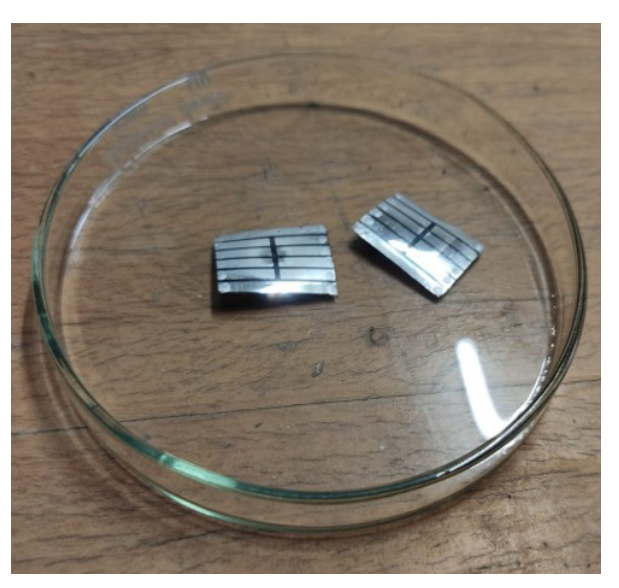
Figure 3.30: IV curve of  $FA_{1-x}MA_xPbI_3$  (coated on PET)

PET is stable upto 80°C temperature, but the annealing temperature goes upto 150°C for the crystallization of  $FA_{1-x}MA_xPbI_3$ . We observed permanent bending in PET substrates after annealing, which causes unwanted expenditure of PET; this may damage to the ITO layer and the pin holes in the perovskite layer. Another problem was to clear the perovskite coating from the edges before Ag deposition. We use a sharp object for this purpose in the case of glass substrate. We used the same approach, but PET is a soft polymer, and any sharp object damages its surface and ITO layer with scratches. We also tried to clean with DMF but after some time we observed holes in the perovskite layer. DMF vapors may diffuse into the perovskite layer and cause this damage. In both of the cases, resistance of ITO was approx  $500\Omega$  which is too large to say that it is conductive.

#### **3.4.3** Trial 2 (failed!)

Keeping in mind the lessons of trial 1, we covered the edges with kapton tape during the coating of SnO<sub>2</sub> and perovskite. In addition, we used a triple cation composition (extensively discussed in Section 3.3) because it needs 100°C for crystallization, which is a safe temperature range for PET substrate. The triple cation also shows the maximum photoresponse in the NIR range.

When annealing the substrates at 90°C after SnO<sub>2</sub> coating, they bended enormously (Fig. 3.31). We tried to coat the following layers but were not able to make a good quality layer of perovskite.







(b) Poor quality of perovskite film

Figure 3.31: Failed fabrication of triple cation composition on PET substrate

## **3.4.4** Trial 3 (succeed!)

Pervious time, we kept PET substrates on hot plate for annealing after the SnO<sub>2</sub> was coated; and substrates were bended. When we keep the substrates on the preheated hot plate, the bottom part of the substrate faces direct heat compared to the other parts. This time we decided to do annealing process in the preheated furnace at 130°C. The whole environment has the same temperature; that is why every part of the substrates receives uniform heat. In addition, we kept the substrates in a glass Petri dish, which is much flatter compared to the surface of the hot plate. Fortunately, we did not face any kind of bending this time on our substrates. Further steps performed very similar as described before. Additionally, we can see the same crack patterns and shiny behavior of the triple cation composition film, which is similar to the glass substrate (Section 3.3).

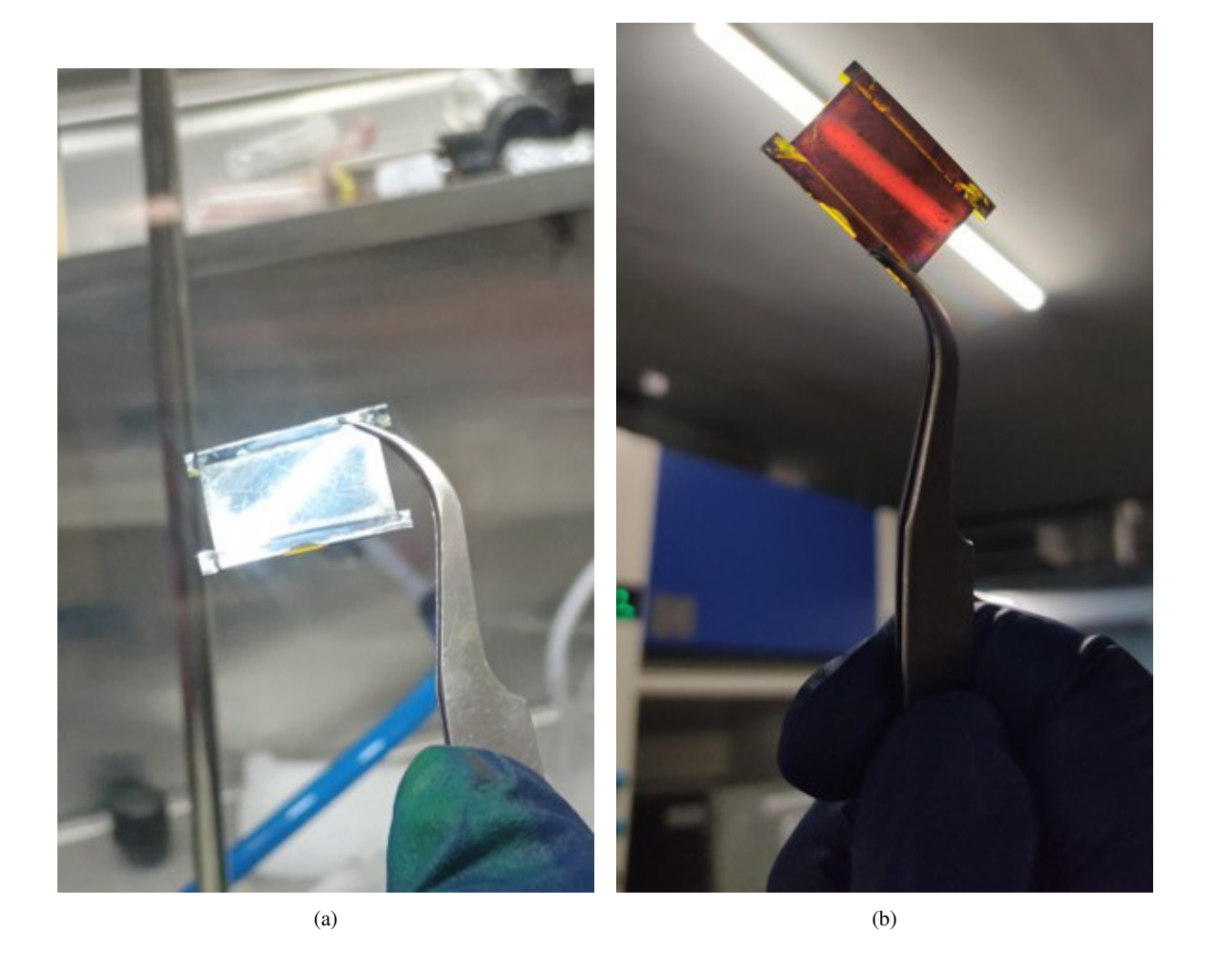
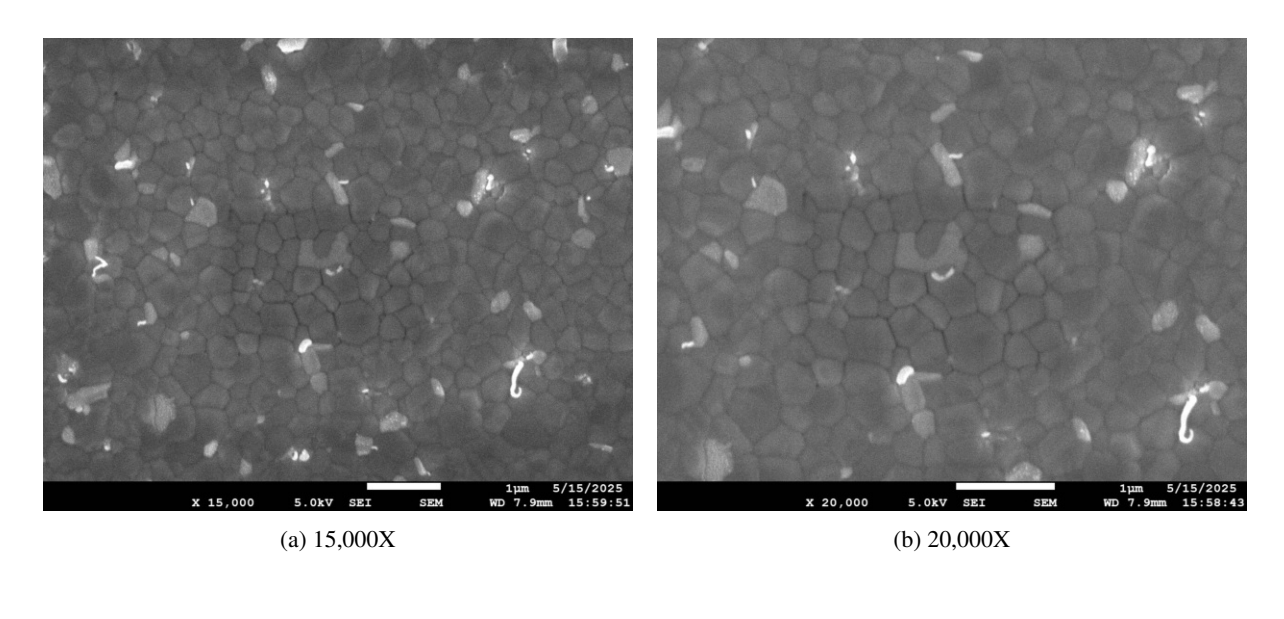


Figure 3.32: Images of well fabricated triple cation Perovskite film on PET substrate

# 3.4.5 Characterization, Results & Discussion SEM:

SEM images shows the perfect crystallization of the triple cation composition on PET substrate. The average grain size was found to be  $0.383_mum$ , here also we found the same results as we obtained from coating of the triple cation on glass substrate. There are some bright grains in Fig. 3.33, this can be the crystals of PbI<sub>2</sub>. Because we took the SEM images after 4 days of fabrication due to unavailability of slots; the sample may undergo degradation during these days.



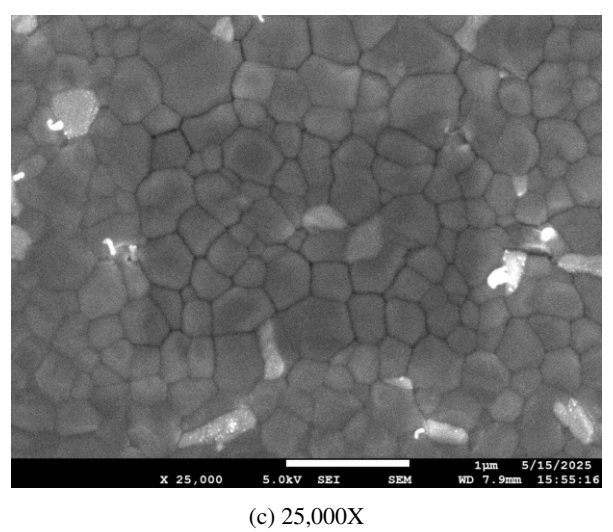


Figure 3.33: SEM images of the triple cation composition coated on PET substrate

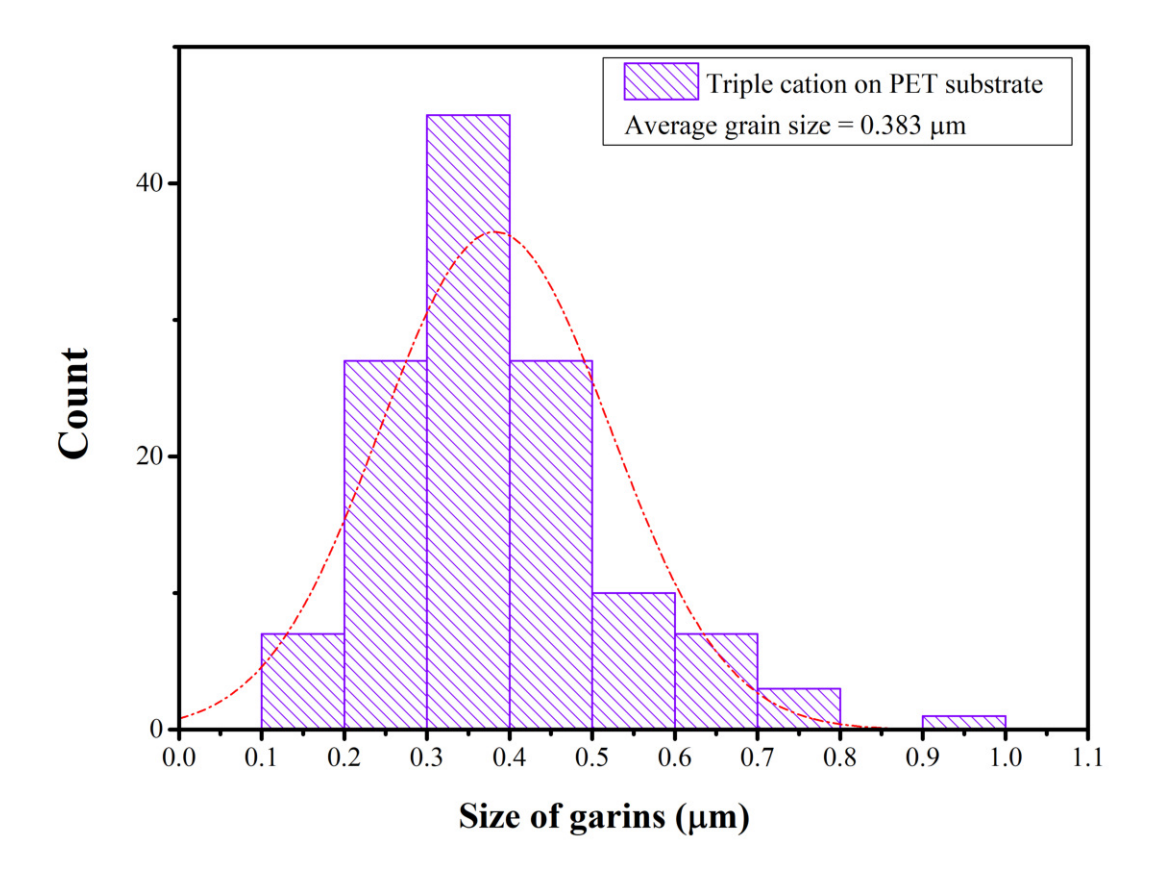


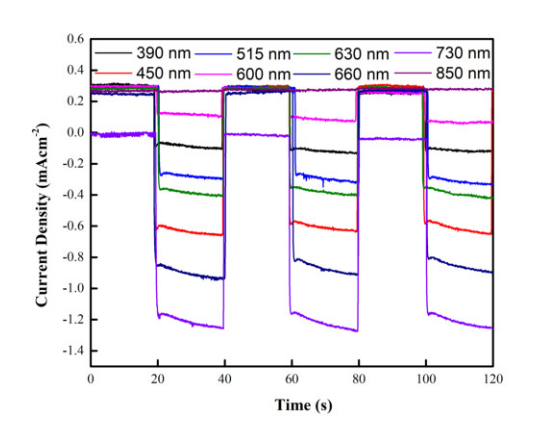
Figure 3.34: Grain size distribution of the triple cation composition coated on PET

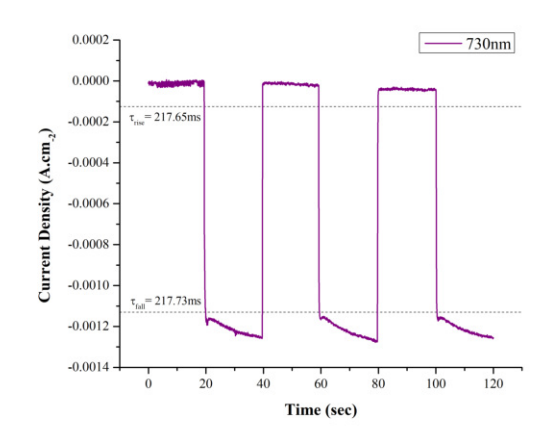
#### **Response time:**

The photoresponse of this PD was recorded at various monochromatic wavelengths by chopping on 20-seconds gap. PD shows a pretty good photocurrent for a wide range of lights, a maximum photocurrent at 730 nm wavelength, and it dies at 850 nm, which was expected. The rise time and fall time calculated accordingly, those were found to be **217.65 ms** and **217.73ms** (Fig. 3.35), respectively. The results are not very different from the triple cation PD fabricated on glass.

#### **Responsivity:**

Responsivity at different wavelengths is plotted in Fig. 3.36. This is better compared to the lateral configuration.





- (a) Photoresponse PD at different wavelengths
- (b) Rise time and fall time of PD at 730nm

Figure 3.35: Photoresponse of triple cation composition PD fabricated on PET substrate

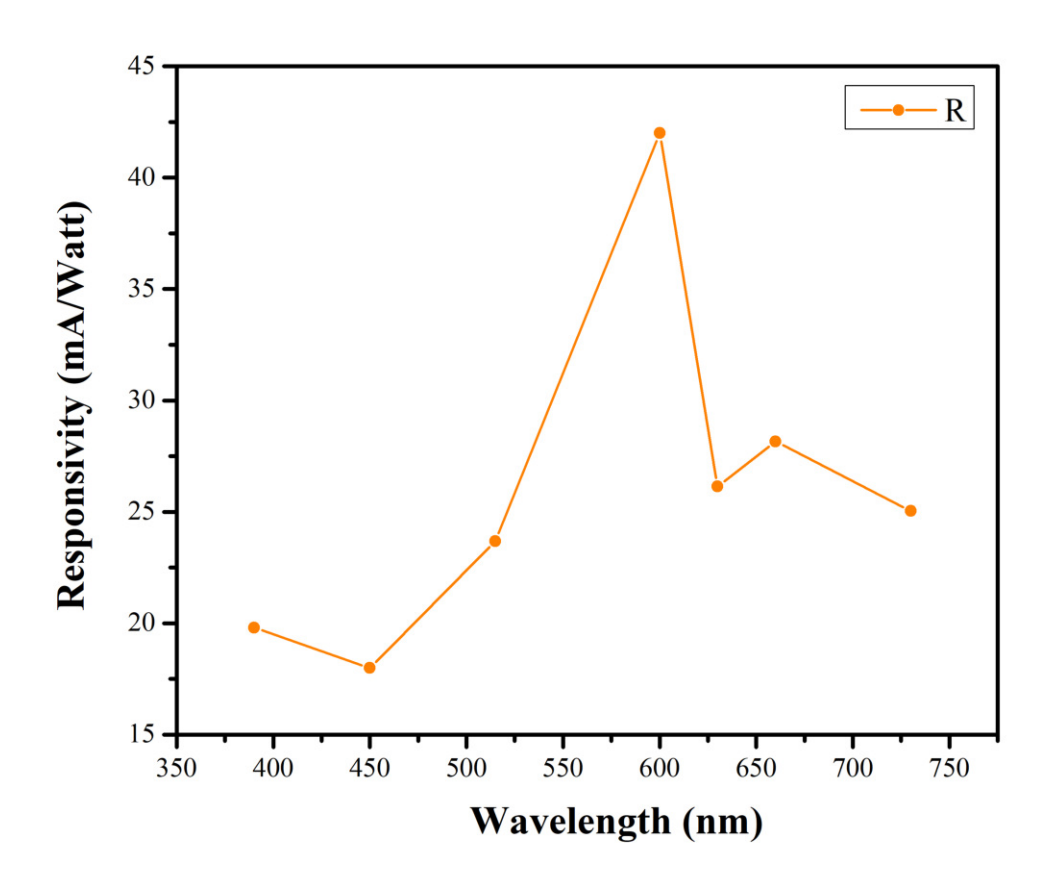


Figure 3.36: Responsivity of the triple cation device fabricated on PET

#### EQE%:

From Fig. 3.37, we can see the EQE peaks for the 600nm wavelength. It is better than the previously lateral configuration device.

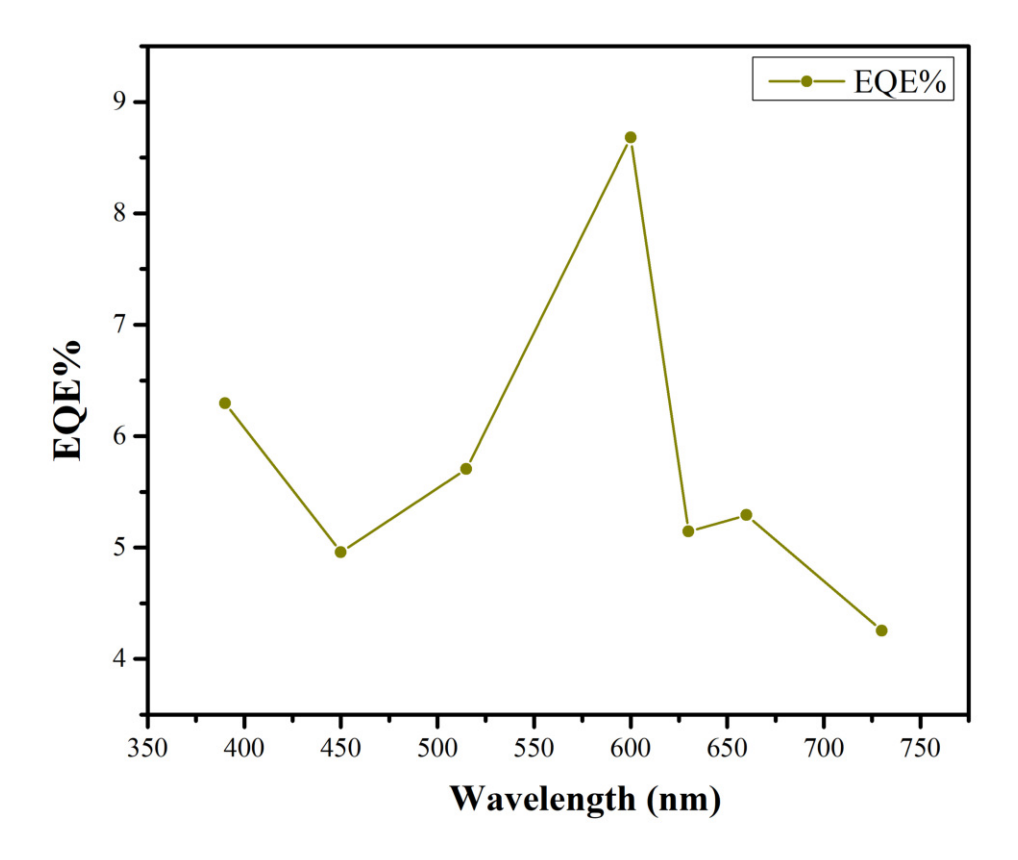


Figure 3.37: EQE of the  $Cs_xFA_{(1-x-y)}MA_yPbI_{3-z}Br_z$  device

# **Specific Detectivity:**

The Specific Detectivity (D\*) of this PD is one order higher (i.e.  $10^6$  than the lateral configuration device (fig 3.38).

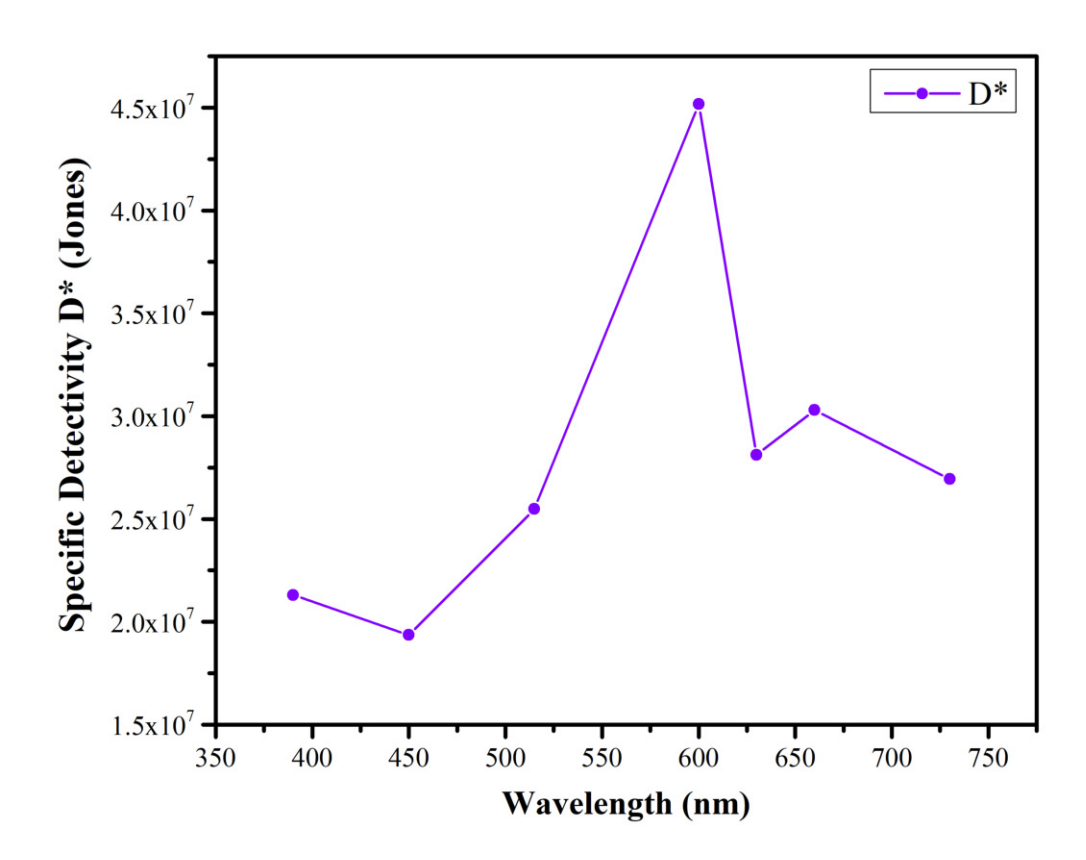


Figure 3.38: Specific Detectivity of the device D\*:

# **Chapter 4**

# **Application (PPG sensor)**

# 4.1 Photoplethysmography

Photoplethysmography (PPG) is a technology that allows one to measure heart rate and oxygen level based primarily on the interaction of light with blood. During heart pumping, the blood volume changes and hence blood concentration changes in the tissues. **This concentration change can modulate light absorption in tissues; this phenomenon is well known, by the "Beer-Lambert law"**; therefore, reflection and transmission of light also change, which can be detected using PD. Oxy-hemoglobin and deoxy-hemoglobin absorb red and IR light, respectively, and this absorption ratio can probe the oxygen saturation level in blood. Modern day pulse oximeters are working on this principle.

Absorption 
$$\propto$$
 Concentration (4.1)

However, this technique is not so new; **it was first developed by Alrick Hertzman in 1937**. He used the Greek world, Plethysmos, which means fullness. He believed that he is measuring the fullness of tissues and made a PPG device for the first time as shown in Fig.4.1 [22].

#### What does a PPG sensor tell?

- Heart-rate
- Stress Level
- Estimated Blood Pressure
- Respiratory Rate
- Blood Oxygen Saturation (SpO2)
- Hypovolemia

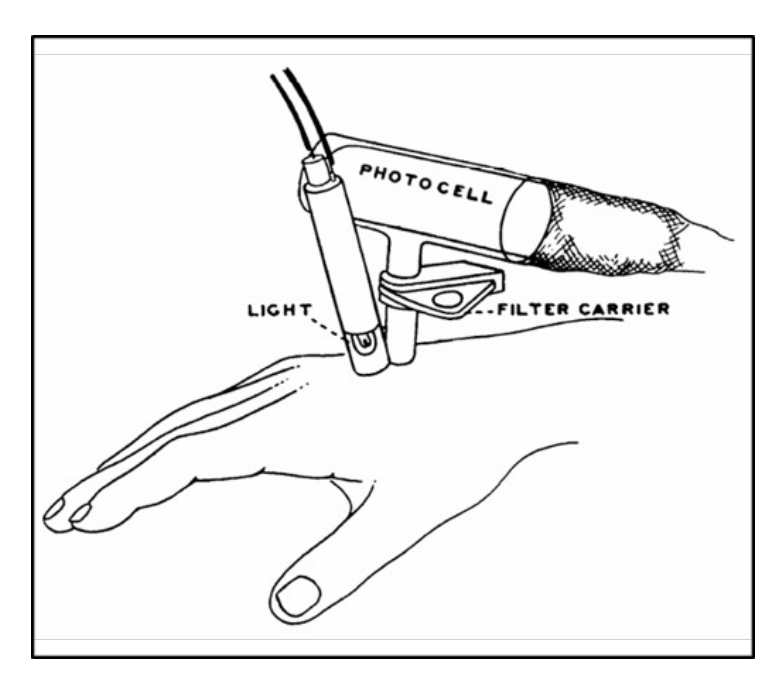


Figure 4.1: The photoelectric plethysmograph, from Hertzman's original setup

Fig. shows a typical PPG waveform[23].

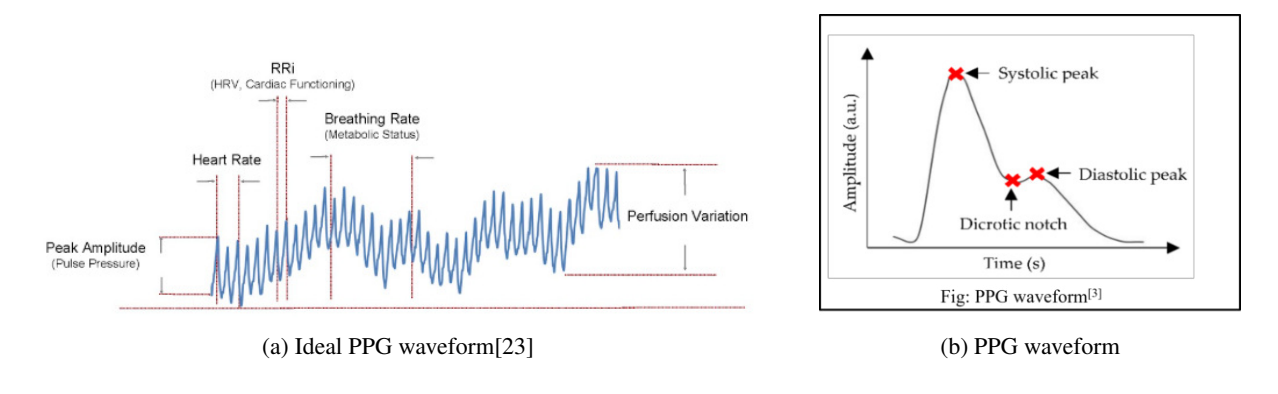


Figure 4.2: PPG waveform

#### 4.1.1 Obtaining PPG waveform by our fexlible PD

We obtain a PPG waveform in transmission mode by placing a figure on the PD and shining a 730nm wavelength light on it (Fig. 4.3). We measured this waveform by the Si photodiode and our prepared flexible PD for cross-verification (Fig. 4.4). Since, we measured both waveform on different days that is why it is showing different heart rate value in the Figure 4.4. It is 88 beats per minute (bpm) for Si-photodiode and 96 bpm for flexible PD. We used keithley 2048 sourcemeter to record this waveform.

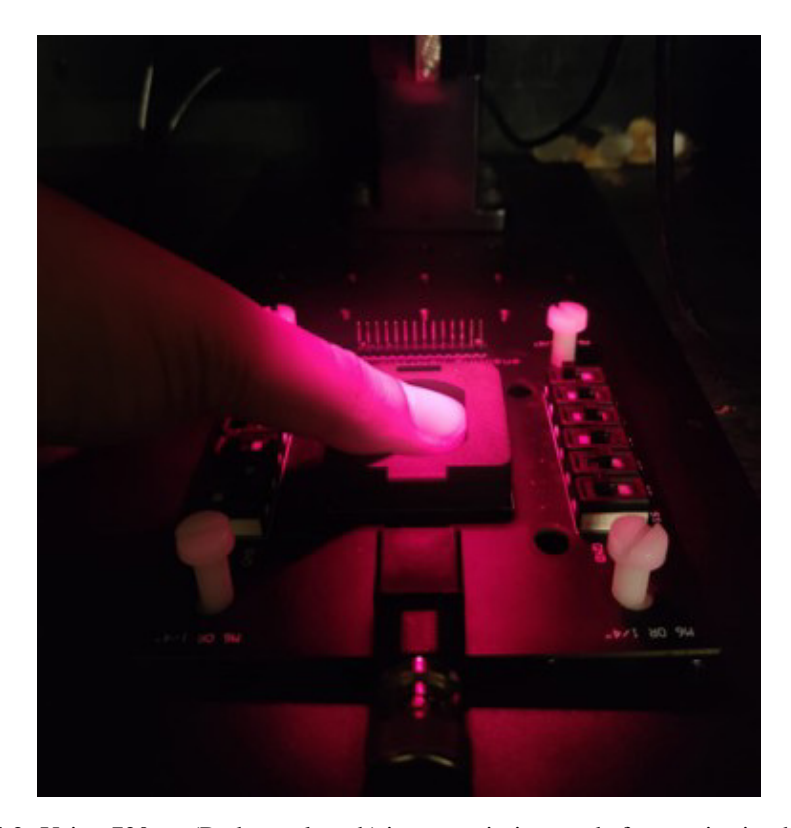
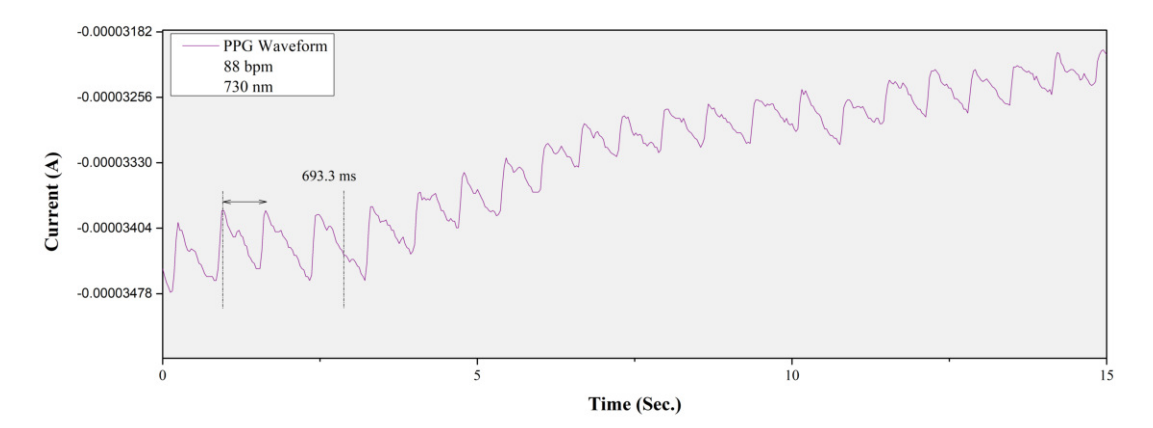
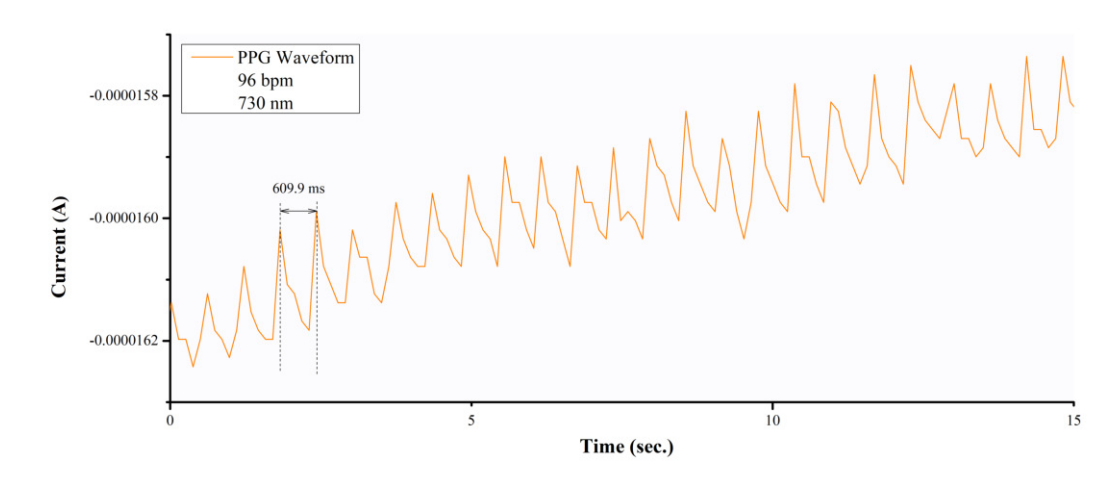


Figure 4.3: Using 730nm (Red wavelength) in transmission mode for monitoring heart rate



(a) PPG waveform obtained by Si photodiode



(b) PPG waveform obtained by flexible PD

Figure 4.4: PPG waveform obtained experimentally

Chapter 5. Conclusion 70

# **Chapter 5**

# **Conclusion**

Although, we have fabricated a complete PD on flexible substrate but, it was unable to show power conversion efficiency under one sun illumination. The triple cation composition is very powerful to perform photovoltaic applications. This suggests that there is still a need for optimizing fabrication steps of a flexible substrate.

However, this work shows the potential to use perovskite thin-films in flexible PD devices. We can utilize this PD as a smart warble gadget after encapsulation and some engineering. This would be an contribution to the filed of wearable electronics and wearable health monitoring device (Fig. 5.1). However, this work completes the targets of this M.Sc. project.

Chapter 5. Conclusion 71



Figure 5.1: Schematic diagram of a smart wearable electronic device[25]

Bibliography 72

# **Bibliography**

- [1] Silvano Donati, *Photodetectors: Devices, Circuits and Applications*, John Wiley & Sons, Inc., Hoboken, New Jersey, 2021.
- [2] X. Zhang, X. Liu, Y. Huang, B. Sun, Z. Liu, G. Liao, T. Shi, Frontiers of Mechanical Engineering 2023, 18:2, 2023, 18, 1.
- [3] https://www.findlight.net/blog/wp-content/uploads/2020/09/working-principle-PMT-768x421.jpg
- [4] https://www.researchgate.net/figure/Thermopiles-sensor-11\_fig6\_ 324907818
- [5] https://www.researchgate.net/publication/310841657/
   figure/fig6/AS:433360628654087@1480332633579/
   Typical-photodetector-time-response-The-device-speed-is-measured-by-a-pulsed-las png
- [6] K. T. Tanko, Z. Tian, S. Raga, H. Xie, E. A. Katz, M. Lira-Cantu, MRS Bull. 2025, 50, 512.
- [7] H. Wang, Y. Sun, J. Chen, F. Wang, R. Han, C. Zhang, J. Kong, L. Li, J. Yang, Nanomaterials (Basel) 2022, 12, 4390.
- [8] Chakhmouradian, A. R.; Woodward, P. M. Celebrating 175 Years of Perovskite Research: A Tribute to Roger H. Mitchell. *Phys. Chem. Miner.* 2014, **41**, 387391.
- [9] A. K. Jena, A. Kulkarni, T. Miyasaka, *Chem. Rev.* 2019, **119**, 3036.
- [10] D. Li, P. Liao, X. Shai, W. Huang, S. Liu, H. Li, Y. Shen, M. Wang, *RSC Adv.* 2016, **6**, 89356.

Bibliography 73

[11] X. Zhang, M. E. Turiansky, J.-X. Shen, C. G. Van de Walle, J. Appl. Phys. 2022, 131, 090901.

- [12] https://www.nrel.gov/pv/cell-efficiency.html.
- [13] C. Perumal Veeramalai, S. Yang, J. Wei, M. Sulaman, R. Zhi, M. I. Saleem, Y. Tang, Y. Jiang, B. Zou, *ACS Appl. Nano Mater.* 2020, **3**, 459.
- [14] Heng, J. L., Luo, C. Z., Shabbir, B., Wang, C. J., Mao, W. X., Zhang, Y. P., Huang, Y. M., Dong, Y. M., Jasieniak, J. J., Pan, C. X., Bao, Q. L., 2019, 11(16): 8020–8026.
- [15] F. F. Targhi, Y. S. Jalili, F. Kanjouri, Results Phys. 2018, 10, 616.
- [16] M. Saliba, T. Matsui, J.-Y. Seo, K. Domanski, J.-P. Correa-Baena, M. K. Nazeeruddin, S. M. Zakeeruddin, W. Tress, A. Abate, A. Hagfeldt, M. Grätzel, Energy Environ. Sci. 2016, 9, 1989.
- [17] H. Li, Y. Zhang, M. Zhou, H. Ding, L. Zhao, T. Jiang, H. Y. Yang, F. Zhao, W. Chen, Z. Teng, J. Qiu, X. Yu, Y. M. Yang, X. Xu, ACS Energy Lett. 2022, 7, 2876.
- [18] C. Bao, W. Xu, J. Yang, S. Bai, P. Teng, Y. Yang, J. Wang, N. Zhao, W. Zhang, W. Huang, F. Gao, Nat. Electron. 2020, 3, 156.
- [19] N. A. Zainal Abidin, F. Arith, N. S. Noorasid, H. Sarkawi, A. N. Mustafa, N. E. Safie, A. S. M. Shah, M. A. Azam, P. Chelvanathan, N. Amin, RSC Adv. 2023, 13, 33797.
- [20] S. Shafique, A. Qadir, T. Iqbal, M. Sulaman, L. Yang, Y. Hou, Y. Miao, J. Wu, Y. Wang, F. Zheng, X. Wang, Z. Hu, J. Alloys Compd. 2024, 1004, 175903.
- [21] L. He, M. Li, Q. Chen, R. Sun, F. Wang, X. Wang, H. Wu, W. Wei, T. Qin, L. Shen, ACS Appl. Mater. Interfaces 2022, 14, 46809.
- [22] A. B. Hertzman, Am. J. Physiol. 1938, 124, 328.
- [23] https://www.youtube.com/watch?v=TyjY4OSEqoo
- [24] S. N. A. Ismail, N. A. Nayan, R. Jaafar, Z. May, Sensors (Basel) 2022, 22, 6195.
- [25] Y. Zhou, X. Qiu, Z. Wan, Z. Long, S. Poddar, Q. Zhang, Y. Ding, C. L. J. Chan, D. Zhang, K. Zhou, Y. Lin, Z. Fan, Nano Energy 2022, 100, 107516.

Bibliography 74

[26] Wu, D. J., Xu, Y. C., Zhou, H., Feng, X., Zhang, J. Q., Pan, X. Y., Gao, Z., Wang, R., Ma, G. K., Tao, L., Wang, H. B., Duan, J. X., Wan, H. Z., Zhang, J., Shen, L. P., Wang, H., Zhai, T. Y. *InfoMat*, 2022, 4(9): e12320.